FOSSIL ENERGY

15
4-16-96(8S1)

DOE/BC/96001222
(DE96001222)

GAS-BUBBLE SNAP-OFF UNDER PRESSURE DRIVEN FLOW IN CONSTRICTED NONCIRCULAR CAPILLARIES

Topical Report

By
A. R. Kovscek
C. J. Radke

April 1996

Lawrence Berkeley Laboratory
University of California
Berkeley, California

Bartlesville Project Office
U. S. DEPARTMENT OF ENERGY
Bartlesville, Oklahoma

DOE/BC/96001222
Distribution Category UC-122

Gas-Bubble Snap-Off Under Pressure Drive Flow in Constricted Noncircular Capillaries

Topical Report

By
A. R. Kovscek
and
C. J. Radke

April 1996

Prepared for
U.S. Department of Energy
Assistant Secretary for Fossil Energy

Thomas B. Reid, Project Manager
Bartlesville Project Office
P.O. Box 1398
Bartlesville, OK 74005

Prepared by
Lawrence Berkeley Laboratory
Earth Sciences Division
and
University of California
Department of Chemical Engineering
Berkeley, CA 94720

TABLE OF CONTENTS

Gas-Bubble Snap-Off Under Pressure Driven Flow In Constricted Noncircular Capillaries

by
A. R. Kovscek and C. J. Radke
Earth Sciences Division of Lawrence Berkeley Laboratory
and Department of Chemical Engineering
University of California
Berkeley, CA 94720

ABSTRACT

A model for snap-off of a gas thread in a constricted, cornered pore is developed. The time for wetting liquid to accumulate at a pore throat into an unstable collar is examined, as is the time for the resulting pore-spanning lens to be displaced from the pore so that snap-off may repeat. A corner-flow hydrodynamic analysis for the accumulation rate of wetting liquid due to both gradients in interfacial curvature and in applied liquid-phase pressure reveals that wetting-phase pressure gradients significantly increase the frequency of liquid accumulation for snap-off as compared to liquid rearrangement driven only by differences in pore-wall curvature. For moderate and large pressure gradients, the frequency of accumulation increases linearly with pressure gradient because of the increased rate of wetting liquid flow along pore corners. Pore topology is important to the theory, for pores with relatively small throats connected to large bodies demonstrate excellent ability to snap-off gas threads even when the initial capillary pressure is high or equivalently when the liquid saturation is low. A macroscopic momentum balance across the lens resulting from snap-off reveals that lens displacement rates are not linear with the imposed pressure drop. Instead, the frequency of lens displacement scales with powers between 0.5 and 0.6 for pores with dimensionless constriction radii between 0.15 and 0.40. Statistical percolation arguments are employed to form a generation rate expression and connect pore-level foam generation events to macroscopic pressure gradients in porous media. The rate of foam generation by capillary snap-off increases linearly with the liquid-phase pressure gradient and according to a power-law relationship with respect to the imposed gas-phase pressure gradient.

INTRODUCTION

Gas injection into oil reservoirs is an important, practical means of improving oil recovery [1] and extending the production lifetime of a reservoir. However, typical gas drive fluids such as steam, carbon dioxide, enriched hydrocarbons, and nitrogen can be inefficient displacement agents because they are much less dense and viscous than the resident oil. Foaming a gas drive fluid is useful for alleviating unwanted buoyancy-driven gas flow and viscous fingering.

In practical applications [2-4] mixtures of surfactant solution and gas are injected into porous oil-bearing rock, and a foam evolves *in situ*. The mechanisms of *in-situ* foam-texture evolution (*i.e.*, the number density of foam bubbles) are not completely elucidated. Specifically, the roles of wetting-liquid flow rate and porous medium capillary pressure on foam generation are not understood. Further, knowledge of foam generation is not complete to the extent that adjustment of bubble size with variations in gas and liquid velocity may be explained quantitatively [5, 6].

Gas bubble formation by snap-off at pore necks is an important mechanism for foam generation [7-10]. Snap-off has been studied in cylindrical capillary tubes and in media that mimic the corners of natural pores such as two-dimensional transparent replicas of rock and constricted, cornered capillaries. Snap-off in cylindrical capillaries has been studied thoroughly both experimentally and theoretically [11-14]. The study most relevant to our work is that of Roof [15]. He considered the snap-off of oil droplets in constricted cylindrical capillaries in which a groove was filed into the capillary wall to enhance liquid flow [15] and developed a static criterion for successful snap-off that states the pore throat to body aspect ratio must be less than roughly 0.5 for snap-off to occur.

Less attention has been given to snap-off in noncircular pores. Observations of snap-off in transparent glass micromodel replicas of rock pore space have revealed a wealth of information on foam behavior. Mast [8] was apparently the first to use a micromodel to study foam generation and flow mechanisms. He recognized that only capillary forces and interfacial tension were involved in snap-off. Chambers and Radke [7] carefully documented and identified the foam generation and destruction mechanisms in micromodels of a Kuparuk (Alaska) sandstone. Owete and Brigham [9] found that bubble snap-off at pore constrictions was the dominant foam generation mechanism in heterogeneous micromodels. However, micromodel studies are not useful for quantifying rates of foam generation because they are dominated by capillary end effects [7]. To quantify snap-off in noncircular pores, Ransohoff *et al.* [16] measured the time to snap-off a gas bubble moving through a smoothly

constricted, square, glass capillary tube at a constant gas flow rate and proposed a companion corner-flow hydrodynamic theory. Interfacial curvature differences were the only driving forces considered for the rearrangement of wetting liquid. Above a critical or transition capillary number, the snap-off time is predicted to be independent of gas velocity. Flow rearrangement of wetting liquid along pore corners determines the snap-off time. Below the transition capillary number, however, snap-off time decreases linearly with the bubble velocity. Experiment satisfactorily matched these predictions.

Falls *et al.* [17] also attempted to quantify snap-off by constructing a rate expression for use in a one-dimensional simulator for foam generation and transport in porous media. They presumed that the time for liquid drainback to pore throats was inversely proportional to a capillary-pressure based (*i.e.*, curvature based) driving force, and that the time for lens displacement was inversely proportional to the interstitial gas velocity. With this rate expression, they were able to match limited experimental foam-flow results from unconsolidated glass beadpacks.

Unfortunately, the above models for snap-off do not address nor explain the dramatic refinement in steady state foam texture that occurs when liquid injection velocity is increased while the gas velocity is held constant [18], or the apparent nonlinear increase in foam generation rate with increasing gas velocity when the liquid injection rate is held constant [6]. As foam texture strongly influences gas mobility in porous media [19], we must understand foam texture evolution in order to understand gas mobility in the presence of foam. Our analysis focuses on foam generation as gas is injected into a porous medium draining wetting liquid and primarily on foam generation at low wetting phase content of the porous medium.

We present a corner-flow hydrodynamic theory to predict the accumulation of wetting liquid preceding the snap-off of a gas thread in smoothly constricted, cornered capillaries with the added feature of an imposed axial liquid pressure gradient. Thus, the rate of accumulation of wetting liquid due to gradients in both interfacial curvature and liquid-phase pressure is calculated. Also predicted is the time required to dislodge the resulting aqueous, pore-spanning lens under the action of a fixed pressure drop so that the snap-off process may repeat. A rate expression for foam generation by snap-off under the action of liquid-phase pressure gradients naturally arises. Such rate expressions are an important ingredient of the mechanistic prediction of foam behavior in porous media reported elsewhere [5, 20, 21].

SNAP-OFF OF GAS BUBBLES

The sequence of events typical of gas-bubble snap-off in water-wet porous media is depicted in Fig. 1 (*c.f.*, [7, 10]) . A thread of gas moves from left to right under the action of a fixed, applied pressure drop. Pore geometry is characterized by a constriction or throat radius, R_c, a body radius, R_b, and a constriction wavelength, L, as displayed in Fig. 2. Note that the pore is gently sloped and smoothly constricted as these are important geometric constraints for foam generation [16]. Figure 2 defines a pore as a throat connected to two adjacent pore bodies.

In Fig. 1a, the gas thread deforms and invades a liquid-filled pore. The interfacial curvature increases as the bubble squeezes into the throat. Gas and liquid pressures on either side of the interface are related through the Young-Laplace equation to both the interfacial curvature and the capillary pressure, P_c,

$$P_c = p_g - p_w = \sigma\, C_m = \sigma\left(\frac{1}{a_1} + \frac{1}{a_2}\right) \qquad (1)$$

where p is the phase pressure, the subscripts g and w represent the gaseous and wetting liquid phases, respectively, σ is the interfacial tension, C_m is the interfacial curvature, and $a_{1,2}$ represent mutually orthogonal interfacial radii of curvature. Two such radii are illustrated in Figs. 2 and 3. $a_\lambda(z_c)$, in Fig. 2, is the transverse or axial interfacial curvature at the pore neck and lies in the plane of the figure, while a, defined in Fig. 3, is the circumferential interfacial curvature that lies in the pore cross section, perpendicular to the plane containing $a_\lambda(z_c)$.

To invade pore throats where liquid fills the entire cross-section or where an aqueous lens spans the pore space, the bubble in Fig. 1a must overcome the entry curvature of the constriction. Numerous equilibrium entry curvatures, $C_{m,e}$, are available in the literature for a variety of pore shapes [16, 22-24]. For a pore with a circular cross-section of radius R, the entry curvature is 2/R corresponding to a hemispherical bubble, whereas for noncircular cross-sections, entry curvatures are slightly less.

After the bubble passes through the pore neck, it expands reducing its interfacial curvature, as illustrated in Fig. 1b. The moving bubble interface rearranges and deposits liquid in the pore corners at a curvature corresponding to the local value of the entry capillary pressure [16, 28, 29]. That is, the interfacial curvature at any axial position is initially determined by the pore size at that position. This gradient in interfacial curvature, between the bubble front and the pore neck, results in a liquid pressure difference that drives

liquid into the pore neck. Additionally, the imposed pressure gradient required to displace the bubble accelerates liquid accumulation at the throat. If enough liquid collects into a collar in a gently sloped pore so that the gas/liquid interface forms an inscribed circle anywhere in cross section in the pore, the collar becomes unstable, since any disturbance in the axial direction grows spontaneously [16]. The result, depicted in Fig. 1c, is snap-off into a pore-bridging lens with a curvature corresponding to the local value of the minimum-surface-energy entry curvature. Thus, a foam lamella is never formed directly by snap-off. After lens creation, gas can reinvade the pore throat displacing the lens, as seen in Fig. 1d. Again, liquid is deposited at the local value of the entry curvature by the moving bubble interface. The snap-off process then repeats so long as ample wetting phase is present and sufficient pressure gradients exist in the gas phase to displace the liquid lens. Eventually, the lens drains to a foam lamella if the capillary-suction pressure is large and surfactant is present to stabilize the thin-liquid film.

Not all pores permit enough liquid to accumulate for snap-off. Depending on the value of R_c/R_b, it may be impossible for enough liquid to collect so that the gas-liquid interface reaches the unstable circumferential inscribed circle configuration. In this situation, the gas/liquid interface reaches a constant curvature, liquid rearrangement in the axial direction ceases, and snap-off does not occur. Rather, a stable liquid collar emerges. For snap-off to occur in a gently constricted pore, the pore throat must fill with liquid such that the interfacial curvature at the pore throat equals the critical curvature for snap-off. Only pore-throat to pore-body constriction ratios, R_c/R_b, of approximately 0.5 or less are sufficiently small to permit collection of enough liquid for snap-off in cornered pores. The critical aspect ratio of pore throat to body size arises from purely static arguments and is known as the Roof criterion [15]. The Roof criterion applies specifically to gently sloped pores where the circumferential curvature is much larger than the axial curvature, and where liquid is initially deposited along pore walls at the local value of the entry curvature. Snap-off is prevented in pores with sharp constrictions because large axial curvatures stabilize the gas/liquid interface against snap-off. Legait [25] actually prevented snap-off of oil experimentally by constructing a sharply constricted square capillary.

An important aspect of Fig. 1 leading to snap-off in porous media are the "nooks and crannies" and corners that line pore walls [7, 26]. A somewhat realistic cross-sectional pore shape is given in Fig. 3a, and a model representation of the shape is presented in Fig. 3b. As the bubble depicted in Fig. 1a moves downstream, wetting liquid remains in the corners of the pores, in addition to coating the pore walls. Thus, Fig. 3 illustrates that substantial

wetting liquid remains in the corners of the pore as compared to the thin films lining the pore walls. Liquid-filled nooks, crannies, and corners typically exhibit much lower hydrodynamic resistance compared to that in the thin-liquid films coating pore walls [16], thereby enhancing the redistribution of wetting liquid.

Figure 1 suggests that snap-off may be divided conceptually into the processes of liquid accumulation, rearrangement of the liquid collar into a pore-spanning lens, and displacement of the lens out of the pore throat. Rearrangement from an unstable collar into a lens is rapid in constricted, circular capillaries [27] and is similarly expected to be rapid in cornered capillaries [16]. Hence, lens rearrangement is not accounted for in light of the longer time scales for liquid accumulation and lens displacement. Liquid accumulation and lens displacement are treated as independent because lens displacement is relatively rapid and does not influence liquid accumulation. In subsequent sections, each time scale is established, and this assertion is verified.

LIQUID ACCUMULATION

Liquid flow along the corners of a pore determines the frequency of liquid accumulation. Because the resistance to flow in thin films scales inversely with the third power of the film thickness, film flow is highly resistive compared to the bulk flow of liquid in pore corners. Consequently, thin films are neglected throughout this analysis as corner flow dominates liquid rearrangement. The secondary effects of thin films on liquid flow in noncircular cross-section capillaries have been proven negligible more rigorously [16]. Hence, calculation of the time required for sufficient liquid accumulation to initiate snap-off amounts to specifying and solving a two-phase corner-flow evolution equation under the action of an imposed liquid-phase pressure gradient.

In addition to neglecting thin films, we also assume that the gas phase is inviscid, flow of the wetting liquid in pore corners is slow and unidirectional, and the wetting liquid is incompressible and Newtonian. Further, the pore is gently sloped and smoothly constricted so that the transverse curvature is negligible relative to the circumferential curvature. Pores with large transverse curvatures are not included in the analysis because they do not permit snap-off and, accordingly, are not relevant to the creation of foam bubbles. For a smoothly constricted pore, the amount of wetting liquid initially deposited in a pore corner is set by the curvature of the bubble front. For slow bubble flow, the interfacial curvature at the front of the bubble is the local value of the equilibrium entry curvature [28, 29].

Continuity of the liquid phase describes the relationship between fluid accumulation and flow rate

$$\frac{\partial A_w}{\partial t} = \frac{-\partial q_w}{\partial z} \tag{2}$$

where A_w is the area of the corner occupied by wetting liquid, and q_w is the volumetric flow rate of wetting liquid. Since the nonwetting gas phase is inviscid, q_w is related to the local liquid pressure gradient through a dimensionless flow resistance, β, for flow corner flow [30]

$$q_w = \frac{a^2(z) A_w}{\mu \beta}\left(\frac{-\partial p_w}{\partial z}\right) \tag{3}$$

In Eq. (3), μ is the wetting liquid viscosity, p_w is the local pressure of the wetting liquid, and a is the circumferential radius of interfacial curvature displayed in Fig. 3. Ransohoff and Radke [30] tabulate β as a function of corner geometry, contact angle, and rigidity of the interface.

We take q_w as the sum of curvature and pressure-driven flows. Any curvature-driven flow to cause rearrangement into a lens or collar is superimposed linearly upon the net transport of wetting liquid through the corners of the pore. The pressure gradient in Eq. (3) is thus the sum of driving forces contributed by differences in interfacial curvature and by the imposed pressure gradient. Since the transverse curvature in Eq. (1) is negligible in comparison to the circumferential curvature for gently sloping pores, the interfacial curvature is 1/a(z), and the total liquid pressure gradient becomes

$$\frac{\partial p_w}{\partial z} = \frac{\sigma}{a^2(z)}\frac{\partial a}{\partial z} + \left(\frac{\partial p_w}{\partial z}\right)_{\text{imposed}} \tag{4}$$

where the last term on the right represents the net imposed pressure gradient. It arises because a pressure gradient is required to drive bubbles through porous media during foam flow, or when gravity is considered for a long vertically oriented pore. Previous work neglected this term [16].

Combining Eqs. (2), (3), and (4) with the observation that A_w is proportional to $a^2(z)$ yields an evolution equation for the interfacial radius of curvature as a function of position and time. In dimensionless form, it reads

$$\frac{\partial \kappa}{\partial \tau} = \kappa \frac{d^2\kappa}{d\zeta^2} + 2\left(\frac{d\kappa}{d\zeta}\right)^2 - Ca_m \kappa^2 \frac{\partial \kappa}{\partial \zeta} \tag{5}$$

Following Ransohoff *et al.* [16], κ (= a/R_b) is taken as the dimensionless interfacial radius of curvature, ζ (= z/L) is the dimensionless axial direction, and τ (= t/t_c) is the dimensionless time. With this choice of scaling, the characteristic time, t_c, is equal to $[2\mu\beta R_b(L/R_b)^2]/\sigma$ and embodies the effects of fluid properties, constriction length, and corner geometry on the time for liquid accumulation. A very viscous fluid or a corner with a large flow resistance factor, β, leads to long liquid accumulation times. Likewise, for low interfacial tensions the characteristic time becomes long. A dimensionless, modified capillary number arises because of the superimposed wetting liquid flow, Ca_m $\left(= \left(\frac{4R_bL}{\sigma}\right)\left(-\frac{\partial p_w}{\partial z}\right)_{imposed}\right)$. It includes factors describing the pore geometry along with viscous and capillary forces. Equation (3) relates the imposed pressure gradient to the viscosity and velocity of the corner fluid, justifying the terminology of a modified capillary number.

Implicit in the derivation of Eq. (5) is the assumption that the flow resistance factor is a constant, independent of position or time. This assumption only holds rigorously for flow in corners of constant cross-sectional shape that are not rounded and for flow where the fluid/fluid interface exhibits either a no-slip or a no-stress boundary [30].

Calculation of the time for liquid accumulation demands a specific pore shape. For illustrative purposes, a pore with a square cross-section and a constriction with the following dimensionless shape function are chosen

$$\lambda(z) = 1 - \frac{(1 - \lambda_c)}{2}\left[1 + \cos(2\pi(\zeta_c - \zeta))\right] \tag{6}$$

where λ = $R(z)/R_b$, λ_c is the dimensionless constriction radius (R_c/R_b), ζ_c defines the dimensionless position of the pore constriction, and $R(z)$ is the largest circle that may be inscribed locally in the pore cross-section. Small dimensionless constriction radii define pores with small throats connected to relatively large bodies. A constriction radius of one refers to an unconstricted tube. A typical pore shape is illustrated in Fig. 2.

Equation (5) is a second-order, boundary-value problem that is solved numerically with a Galerkin finite element method using Newton-Raphson iteration to resolve the nonlinearities. Crank-Nicolson time stepping provides an algorithm that is unconditionally

stable and second-order accurate in time. Further numerical details are available elsewhere [31]. Both constant curvature and no-curvature-driven-flux boundary conditions are relevant to the pore-level physics of snap-off. No-curvature-driven-flux boundary conditions at both pore boundaries restricts a pore, in a serially connected set of pores, to only rearrange the initial volume of liquid within one pore wavelength. Here, $\partial\kappa/\partial\zeta$ is zero at the pore boundaries, ζ = 0 and 1. For simplicity, this is termed a no-flux boundary condition throughout the remainder of the paper. Liquid, though, streams along the liquid-filled corners of the pore in response to the imposed pressure gradient. A constant curvature boundary condition (*i.e.*, constant capillary pressure suction) is akin to connecting a pore body to a large source of wetting liquid. Liquid is supplied at the pore boundaries without changing the gas/liquid curvature at those boundaries, or κ = constant at ζ = 0 and 1.

In the first calculations, the curvature of the gas/liquid interface in the center of the pore bodies adjacent to a pore throat is fixed to the entry curvature, consistent with a pore that is connected to a liquid source. The initial condition is liquid deposited in pore corners with a curvature determined by the entry curvature at the local, axial pore size consistent with repeated snap-off and rearrangement of corner liquid by a moving lens. Liquid accumulation continues until the interface assumes an inscribed circle (*i.e.*, unstable) configuration anywhere within the pore, or until a constant curvature (*i.e.*, stable) interface forms throughout the pore. Snap-off always occurs near the pore throat because the interfacial curvature is greatest there. The dimensionless time, t_a, to accumulate enough liquid for snap-off in a square constricted pore is plotted versus the dimensionless constriction radius in Fig. 4 for Ca_m = 0, 10, 50, and 100. These modified capillary numbers correspond to imposed pressure gradients of 0, 400, 2000, and 4000 kPa/m (0, 17.7, 88.5, and 177 psi/ft), respectively, for a pore with a pore-body radius of 100 μm, a normalized constriction length (L/R_b) of 20, and where the interfacial tension is 32 mN/m. The amount of time required for liquid accumulation prior to snap-off decreases dramatically with increasing Ca_m. At large modified capillary numbers, liquid is pumped rapidly through the pore corners, due to the large imposed pressure gradient, and quickly accumulates at the throat.

Interestingly, the curves for Ca_m equal to 50 and 100 asymptote sharply at a dimensionless constriction radius of roughly 0.53 which corresponds exactly to the Roof criterion [15, 16] for a pore with a square cross-section. This limit is indicated by the dashed line on Fig. 4. In the limit of no imposed pressure gradient, Ca_m = 0, liquid accumulation times in a cornered capillary increase with λ_c because the pore walls are not sufficiently

curved to draw liquid rapidly into the pore throat for snap-off. At high imposed pressure gradients, however, liquid is pumped quickly into growing collars accelerating the curvature-driven rearrangement of liquid, even when interfacial curvature gradients are not large. For λ_c greater than the Roof criterion, snap-off is always prohibited because the corner liquid assumes a constant curvature shape and profile rearrangement of the corner liquid ceases before reaching the unstable collar configuration.

For an infinitely tight constriction where λ_c equals zero, t_a remains finite. As first explained by Ransohoff *et al.* [16] for snap-off in cornered pores, as λ_c approaches zero, the snap-off position is slightly downstream from the pore neck at a dimensionless axial position of 0.05. Hence, the accumulation time must remain nonzero.

In the second example reported in Fig. 5, a no-flux boundary condition is applied in the center of the pore bodies adjacent to a pore throat. Again, the initial liquid profile is given by the local value of the equilibrium entry curvature. The gas/liquid interfacial curvature is symmetric about each pore boundary, and liquid in the pore corners simply rearranges. For highly constricted pores, the result is identical to the results in Fig. 4. However, for λ_c greater than roughly 0.35 and Ca_m equal to zero, the times for snap-off in Fig. 5 increase more rapidly with increasing λ_c than in Fig. 4. Again the dashed, vertical line denotes the Roof criterion for this pore shape. As the pore throat becomes less constricted, it takes a very long time to accumulate the liquid available within one pore wavelength into an unstable collar. For only curvature-driven rearrangement of liquid (*i.e.*, $Ca_m = 0$), a square pore with a constriction to body ratio greater than about 0.4 does not snap-off. The pore is starved for liquid even though the static Roof criterion indicates that snap-off may occur. A collar forms, but the critical curvature for snap-off cannot be reached. As Ca_m increases from 0 to 100, we again see that the time for snap-off decreases dramatically. Additionally, for Ca_m of 50 and 100, the strong imposed pressure gradients allow snap-off to occur at the Roof criterion, where t_a asymptotes sharply.

In the third example, we explore the competing effects of pore drainage due to capillary suction and liquid accumulation at the pore throat by calculating snap-off in pores that attempt to establish equilibrium with the overall porous-medium capillary pressure. The initial liquid profile is still set by the local value of the equilibrium entry curvature except at the pore boundaries where the capillary pressure or curvature is set to a value greater than that given by the equilibrium entry value. Hence, the constant curvature at pore boundaries is fixed by the medium capillary pressure, and liquid drains from the pore in addition to spontaneously rearranging. Ca_m is first set to zero, so that we examine purely curvature-

driven liquid rearrangement while the pore-boundary curvature is made progressively larger.

Figure 6 presents liquid accumulation times as a function of the pore constriction size and the capillary pressure condition applied at the pore boundaries. Curves are labeled with a ratio of capillary pressures, $P_{c,b}/P_{c,e}$, to indicate the capillary pressure at the boundary relative to the equilibrium capillary entry pressure. The subscripts b and e indicate the boundary and entry capillary pressures, respectively. A ratio of unity states that liquid at the pore boundary is at the local equilibrium entry value of the capillary entry pressure for a given pore size. Ratios greater than unity indicate that the local boundary capillary pressure is greater than the entry capillary pressure. Note that we probe capillary pressures almost twice the equilibrium entry value. Figure 6 makes two important points. First, with increasing values of $P_{c,b}/P_{c,e}$ the critical pore-throat to body aspect ratio necessary for sufficient liquid accumulation for snap-off decreases. That is, the range of pores supporting snap-off narrows toward pores with relatively small throats as the boundary capillary pressure increases. Second, for those pores that have small pore throats relative to their body size, the time for accumulation of liquid and snap-off to a pore spanning lens in all cases is almost identical to the $P_{c,b}/P_{c,e}$ equal to 1 case until the dimensionless radius of constriction closely approaches a critical value, λ^*, separating pores that snap-off from those that do not.

The critical pore-throat to body ratios in Fig. 6, where accumulation times asymptotically approach infinity, are given by a restatement of the Roof criterion [15, 16] incorporating the interfacial curvature at the boundary. The Roof criterion is purely static and relates the critical inscribed circle configuration of wetting fluid necessary for snap-off to pore geometry. It assumes that the curvature of liquid in pore corners at the boundaries is at the (dimensionless) entry curvature and states that this curvature controls snap-off. To obtain an analytic expression for the geometric criterion for snap-off represented by the asymptotes in Fig. 6, we replace the entry curvature with the dimensionless boundary curvature in Eqs. (3) to (7) of Ransohoff *et al.* [16]. For the case of a gently sloping pore, the following static criterion incorporating pore geometry emerges

$$\lambda_c \leq \lambda^* = \left(\frac{P_{c,b}}{P_{c,e}}\widetilde{C}_{m,e}\right)^{-1} = \left(\widetilde{C}_{m,b}\right)^{-1} \qquad (7)$$

where $\widetilde{C}_m$ (=$C_m R_b$) is the nondimensional curvature. Equation [7] recovers the Roof criterion when the boundary curvature equals the equilibrium entry curvature. The two vertical dashed lines on Fig. 6 represent the usual Roof criterion for $P_{c,b}/P_{c,e}$ equal to 1 (*i.e.*, $\lambda^* = 0.53$) and the modified criterion given by Eq. (7) for $P_{c,b}/P_{c,e}$ equal to 1.4 (*i.e.*, $\lambda^* = 0.38$). Table 1 lists all of the critical aspect ratios for the square-tube calculations summarized in Fig. 6. In all cases, the numerical calculations closely approach the asymptotes predicted by Eq. (7).

Figure 7 gives liquid accumulation times for increasing superimposed liquid phase pressure gradients when $P_{c,b}/P_{c,e}$ equals 1.4. The vertical dashed line again represents the snap-off criterion stated by Eq. (7). Similar to both Figs. 4 and 5, the time required for liquid accumulation prior to snap-off decreases dramatically with increasing Ca_m. Trends similar to those presented in Fig. 7 for increasing values of Ca_m are obtained for all reasonable values of the ratio $P_{c,b}/P_{c,e}$.

Interestingly, comparison of Figs. 4 through 7 teaches that similar results are obtained for tightly constricted pores under a variety of imposed liquid-phase pressure gradients and initial and boundary conditions. Liquid accumulation is so rapid for tightly constricted pores that the initial and boundary conditions do not influence strongly the accumulation time. We do not perform calculations of accumulation time for pores with both drainage due to capillary suction and no-flux boundary conditions as this case is aphysical .

LENS DISPLACEMENT

Final rearrangement of the accumulated liquid in an unstable collar into a pore-spanning lens is very rapid [27]. Before liquid accumulation commences again, however, the lens must be displaced from the pore throat. Expulsion of the lens requires that the pressure drop across the lens be sufficient to overcome all viscous and capillary resistances present. To follow the unsteady motion of the lens depicted in Fig. 8, we apply a macroscopic momentum balance. Consistent with our assumption of rapid lens displacement times as compared to transport times of liquid along pore corners and surface roughness, we assume that the lens has little time to drain and maintains constant volume. The lens control volume lies between the curved lens surfaces 1 and 2, as indicated by the shading in Fig. 8, and moves with the lens. This control volume is useful in that momentum influx and efflux are eliminated for a lens of constant volume.

Consistent with the previous assumptions of a gently sloping pore and slow flow, the

lubrication approximation applies and the velocity of the liquid in the lens is coparallel with the pore axis. That is, the magnitude of the velocity is identical to the axial component of the velocity. The lens slides over both the thin lubricating films lining the pore walls and the bulk wetting fluid in the pore corners.

Under these restrictions, the axial component of the momentum balance [32, 33] for the situation depicted in Figure 8 is written as

$$\rho \frac{d}{dt} \int_V U(z)\, dV = p_{w1} A_1 - p_{w2} A_2 + F_p - F_D \tag{8}$$

where ρ is the liquid mass density, U is the average axial lens velocity as a function of the axial position, V is the (constant) lens volume, p_{w1} and p_{w2} are the respective average liquid pressures at surfaces 1 and 2, and A_1 and A_2 are the axially projected areas of surfaces 1 and 2, respectively. The left side of Eq. (8) represents the accumulation of momentum in the control volume. The first two terms on the right describe the entrance and exit pressure forces acting at surfaces 1 and 2, respectively, while F_p arises from the pressure exerted by the capillary wall on the lens fluid and F_D describes the axial viscous drag encountered by the lens.

To obtain the entrance and exit pressure forces, a force balance is performed to relate the gas pressures across the lens interfaces to the liquid pressures at surfaces 1 and 2. Thus, the pressure difference across each liquid/gas surface of the lens reads [28] :

$$(p_{g1} - p_{w1}) A_1 = (\sigma 2\pi R_1 + D_{f1}) \cos\omega_1 , \tag{9a}$$

and

$$(p_{g2} - p_{w2}) A_2 = (\sigma 2\pi R_2 + D_{f2}) \cos\omega_2 \tag{9b}$$

where R is the radius of the largest circle that can be inscribed locally in the pore cross-section, and ω is the angle between the radius of interfacial curvature, a, and R. The subscripts g1, w1, g2 and w2 refer to the gas and liquid pressures immediately adjacent surfaces 1 and 2, respectively. Equation (9) applies for a tube of any cross-section. For a straight tube, ω is zero. The drag force, D_f, arising from moving a meniscus over a thin liquid film is given by Wong *et al.* [28]

$$D_{fi} = 2\pi R_i \sigma \alpha_i \, Ca_i^{2/3} \ , \ i = 1,2 \qquad (10)$$

where α is a constant of proportionality that is different for the front and rear of the lens, σ is the surface tension, and Ca ($=\mu U(z)/\sigma$) is the local capillary number. The continuity equation

$$A_1 U_1 = A(z)U(z) \qquad (11)$$

relates the average velocity, U(z), anywhere inside the lens to the average velocity at the projected area of surface 1. Equations (9) and (10) give the liquid pressure at surfaces 1 and 2 as a function of the gas pressure and the interface velocity.

The viscous force exerted by the lens fluid in unidirectional flow on the wall of a capillary with a general cross-sectional shape is

$$F_D = \int_{wall} \mu \left(\frac{\partial v_z}{\partial r} \right)_{R(z)} dA_{wall} \qquad (12).$$

where A_{wall} is the wall area wetted by the lens. The derivative of the axial velocity, $v_z(r)$, is evaluated at the pore wall.

To obtain the pressure force acting in the axial direction, the local lens pressure is multiplied by the axial differential area, the product is then projected in the z-direction and integrated. For gently sloping pores, the projection in the z-direction is, to an excellent approximation, the slope of the pore wall, dR/dz. Thus, the pressure force is written as

$$F_p = \int_{wall} p_w(z,r) \frac{dR}{dz} dA_{wall} \qquad (13)$$

In the lens-displacement calculations to follow, a circular constricted pore is chosen because it provides a simple geometry and because the drag and fluid pressure relationships are known exactly. Pore geometry is not crucial for obtaining the flow-rate trends of lens displacement, because flow resistances for bubble or lens flow in slots, and in pores with circular and noncircular cross-sections scale with velocity in a similar fashion [28, 34]. The pressure drop to drive a bubble or lens scales as $Ca^{2/3}$ consonant with the classical result of Bretherton [35]. Only the proportionality constants differ among differing pore geometries. In

fact, Wong *et al.* [28] derive the proportionality constants, α, for a variety of polygonal pore shapes, such as triangles, squares, and hexagons, and find that the proportionality constants are all approximately equal and about a third of the circular-pore proportionality constant. Thus, a circular constricted pore provides a conservative estimate of lens displacement times while maintaining the proper velocity scaling.

For a circular constricted pore, where lens flow is described by local Poisueille flow, the integrals in Eqs. (12) and (13) have been evaluated elsewhere (*cf.*, Eqs. (6) and (13) of ref. [32]). Substitution of Eqs. (9) through (13) into Eq. (8) yields an expression describing the position of the upstream plane of the lens as a function of time for a given pressure drop, parameterized by the lens volume and the pore shape:

$$\frac{d}{d\tilde{t}}\left[\lambda_1^2(h_2 - h_1)\frac{dh_1}{d\tilde{t}}\right] = \lambda_2^2(\tilde{p}_{g1} - \tilde{p}_{g2}) + 2\lambda_2\left(\cos\omega_2 - \frac{\lambda_2}{\lambda_1}\cos\omega_1\right)$$
$$-Oh\lambda_1^2(16S_2 + 8S_1)\left(\frac{dh_1}{d\tilde{t}}\right) \qquad (14).$$
$$+ 2\lambda_2 Oh^{2/3}\left[\alpha_1\frac{\lambda_2}{\lambda_1}\cos\omega_1 - \alpha_2\left(\frac{\lambda_1^2}{\lambda_2^2}\right)^{2/3}\cos\omega_2\right]\left(\frac{dh_1}{d\tilde{t}}\right)^{2/3}$$

In the accumulation term, Eq. (11) is utilized, and the result is integrated over the lens volume. In Eq. (14), dimensionless time, $\tilde{t}$, is defined by $t/(\rho R_b^3/\sigma)^{1/2}$ where the denominator is an inertial time scale, h ($=z/R_b$) is the dimensionless axial position where h equal to zero defines the location of the pore throat, and $\tilde{p}_g$ ($=pR_b/\sigma$) is a scaled gas-phase pressure. The Ohnesorge number, $Oh = \mu/(\rho\sigma R_b)^{1/2}$, gauges the relative importance of inertia. Small values of Oh lead to impulsive, jerky lens motion, known as Haines jumps [36], whereas large values yield smooth, continuous lens displacement. h_1 is the axial location where the upstream lens meniscus intersects the pore wall.

S_1 and S_2 are dimensionless pore-shape integrals with the following definitions

$$S_1 \equiv \int_{h_1}^{h_2} \frac{dh}{\lambda^2(h)} \qquad (15),$$

and

$$S_2 \equiv \int_{h_1}^{h_2} \left[\int_{h_1}^{h} \frac{d\xi}{\lambda^4(\xi)} \right] \lambda \frac{d\lambda}{dh} dh \qquad (16),$$

where ξ is a dummy variable of integration.

Briefly, the first term on the right of Eq. (14) describes the force exerted on the lens by the difference in gas pressure on either side of the lens. The second term represents the contribution of surface tension to the net force on the lens. Depending on the position of the lens in the pore, this contribution may aid aid or hinder lens movement. The third and fourth terms are drag contributions from displacing the bulk fluid in the lens and displacing the lens menisci, respectively.

Equation (14) is a second-order initial value problem that is readily solved by Runge-Kutta methods [37]. A fourth-order method is used here [31]. The trapezoidal rule is used to evaluate the pore-shape integrals. Calculation of the time for lens displacement proceeds once a dimensionless lens volume $\tilde{V}$ (= V_{lens}/R_b^3), pore geometry, and pressure driving force $\Delta\tilde{p}$ (= $\tilde{p}_{g1}$ - $\tilde{p}_{g2}$) are specified. Following rearrangement of a liquid collar into a lens, the lens is initially stationary. Hence, the initial condition for computations is U (=$dh_1/d\tilde{t}$) equal to zero. The proportionality constants for contact line drag, α_3 and α_4, are assigned smooth tube values of 3.8785 and 1.13065, respectively [28]. The Ohnesorge number is fixed at 0.021 for computations. This value corresponds to lens fluid with a viscosity of 1.2 mPa-s, density of 1000 kg/m^3, an interfacial tension of 32 mN/m in a tube with an R_b of 100 μm. Finally, Eq. (6) again describes the axial pore shape.

Figure 9 displays a typical plot of dimensionless time versus position of the upstream location where the lens meniscus contacts the wall, h_3 (displayed schematically on Fig. 8), as a solid line. Also inserted is a schematic of the pore and the initial position of the lens. The pore is quite constricted and long with a dimensionless constriction radius of 0.20 and a constriction length, L/R_b, of 20. Recall that pores with sharp constrictions (for example, L/R_b = 1) prohibit snap-off because the sharp transverse interfacial curvature stabilizes the interface. Initially, the lens is centered about the constriction with h_3 at a position of about -4. The lens moves slowly as the rear of the lens squeezes through the constriction. Once past the constriction, the lens moves quickly through the pore body, and again slows down at about h_3 equal to 14 in order for the trailing lens interface to squeeze through the next pore

constriction. Rapid lens translation through the pore body is similar to a classic Haines jump [36]. The lens repeatedly slows down and speeds up as it transports through subsequent pore throats and bodies.

Figure 10 summarizes the dimensionless time, t_d, to push a lens out of a pore constriction to h_3 equal to 10 in Fig. 9, as a function of the pore throat to body size ratio for a variety of dimensionless pressure drops. Dimensionless lens volume is identical to that in Fig. 9, as are the constriction length and Ohnesorge number. The asymptotic increase in displacement time for tight constrictions at each pressure drop reveals that a threshold pressure drop must be exceeded to overcome capillary forces that tend to drive lenses into pore throats. This threshold pressure drop gives the minimum value that must be exceeded in order to mobilize a lens and dislodge it completely from a pore throat. Otherwise, the lens remains stationary in the pore throat or slightly downstream of the throat where the imposed pressure drop is just balanced by capillarity. Setting the velocity terms in Eq. (14) to zero teaches that $\Delta\tilde{p}$ must always be greater than $2(\lambda_1^{-1}\cos\omega_1 - \lambda_2^{-1}\cos\omega_2)$ for successful lens mobilization. It is clear that the threshold pressure drop depends on the constriction geometry and the volume of fluid in the lens. As expected, the threshold pressure drop decreases for less constricted pores, and the time for lens displacement decreases with increased pressure drop.

Our model of lens displacement has three dimensionless parameters that may be varied in addition to dimensionless pressure drop and the ratio of pore throat to body size. First, displacing a lens of greater volume incurs more viscous drag at the wall increasing the lens displacement time for any given pressure drop. Second, decreasing the length of the constriction decreases the lens displacement time. Third, decreasing Oh decreases the total time a lens spends moving through a pore, and decreases the time the lens spends traversing a pore body relative to the time required to squeeze past a pore throat. As Oh decreases, lens motion is impulsive and rapid, whereas for large Oh (O(0.1)), lens motion is smooth.

RATE OF FOAM GENERATION BY SNAP-OFF

We desire a pore-level based rate expression for snap-off and a connection of pore-level foam generation to macroscopic gas and liquid flow in porous media. Earlier studies [16, 17, 38] argue that the rate of foam generation is inversely proportional to the time to snap-off a gas bubble with the proportionality constant reflecting the number of active foam germination sites. Ransohoff *et al.* [16] take the maximum of the dimensional accumulation or

displacement time as the time for snap-off, whereas others [17, 38] take the snap-off time as the sum of accumulation and displacement times. We explore a statistical model for translating the pore-level snap-off results into a porous medium rate expression. First, though, we establish the pore-level frequency of accumulation and lens mobilization. Implicitly, our analysis assumes that liquid accumulation and lens displacement in assemblies of connected pores are not highly cooperative phenomena.

Liquid-Pressure-Gradient Dependence

The frequency of liquid accumulation to form a collar that subsequently rearranges into a lens is a function of the imposed pressure gradient within a given pore. Additionally, the capillary pressure of the porous medium is an important parameter. Figure 11 demonstrates the dimensionless frequency of liquid accumulation as a function of imposed pressure drop for constant curvature boundary conditions. Liquid is initially arrayed with a curvature corresponding to the local value of the equilibrium entry value for a variety of constriction aspect ratios. We find that f_a essentially increases linearly for modified capillary numbers greater than about 5. Each curve has a finite intercept because interfacial curvature gradients cause liquid accumulation even when no pressure gradient is imposed through the wetting corner liquid. Experimental confirmation of the magnitude of the intercept and the limiting behavior as Ca_m approaches zero is provided by the data of Ransohoff et al.[16] for gas-bubble snap-off in single, square tubes. To achieve this comparison, bubble capillary numbers must be rescaled to our Ca_m using the theory of Wong et al [28] for bubble flow in cornered capillaries. Additionally, application of no-flux boundary conditions to the calculations summarized in Fig. 11 produces qualitatively similar results [31].

Figure 12 displays f_a versus Ca_m as the curvature of the interface at the boundaries of a pore increases. The pore throat to body aspect ratio is fixed at 0.40. The linear trend of increasing f_a at moderate to high modified capillary numbers in Fig. 11 is maintained as the fixed boundary capillary pressure is increased. The role of decreasing pore boundary curvature is to decrease the frequency of accumulation and increase the range of Ca_m over which the accumulation frequency is nonlinear. Further, the trends displayed in Fig. 12 generalize to pores of differing constriction size.

Figures 11 and 12 suggest the following functional form for f_a

$$f_a = f_{a,o}(\lambda_c, P_{c,b}/P_{c,e}) + B(\lambda_c, P_{c,b}/P_{c,e})\, Ca_m \qquad (17)$$

where $f_{a,o}$ is the accumulation time when no pressure gradient is imposed, and B is the slope of the curve. As λ_c decreases, $f_{a,o}$ increases because liquid is drawn rapidly toward the pore throat. On the other hand, $f_{a,o}$ decreases for a fixed λ_c as the capillary pressure at the pore boundary increases (hence, the ratio $P_{c,b}/P_{c,e}$ increases). Competition between liquid accumulation and drainage reduces $f_{a,o}$ for a given λ_c. Likewise, B depends on λ_c and $P_{c,b}/P_{c,e}$. The slope increases slightly with decreasing dimensionless constriction radii, because tightly constricted pores demand a more rapid frequency of liquid accumulation, but decreases as $P_{c,b}/P_{c,e}$ is increased at a fixed constriction aspect ratio due to the decreased availability of liquid. Equation (17) applies strictly to Ca_m above about 5, but it well approximates the low Ca_m regime also. Deviation from linearity occurs at low capillary numbers because strongly constricted pores rearrange liquid rapidly due to pore wall curvature, even when the imposed liquid pressure gradient is small and $P_{c,b}/P_{c,e}$ is high.

Gas-Pressure-Drop Dependence

Figure 13 displays the reduced frequency of lens displacement, on a log-log scale, as a function of the reduced pressure drop, $\Delta\tilde{p}$ - $\Delta\tilde{p}_T$, where $\Delta\tilde{p}$ is the imposed pressure drop across the lens and $\Delta\tilde{p}_T$ is the threshold pressure for a given constriction radius, geometry, and lens volume. The inertial time scale has been converted to the same as in Figs. 11 and 12 by dividing by Oh. The frequency of lens displacement increases with the constriction aspect ratio, since it is easier for lenses to squeeze out of less constricted pore throats. The linearity of the numerical results indicates a power-law dependence such as

$$f_d = D(\lambda_c)\left[\Delta\tilde{p} - \Delta\tilde{p}_T(\lambda_c, L/R_b, \tilde{V})\right]^{\eta(\lambda_c)} \qquad (18)$$

where the line for each dimensionless constriction ratio follows a slightly different power-law relation, with η and D depending on λ_c. The power-law exponent decreases with increasing λ_c, because the time interval spent moving the lens out of the pore throat to the point where the Haines jump through the pore body begins, decreases with both increasing λ_c and increasing reduced pressure drop. Tightly constricted pores are more dissipative than less constricted pores. The time required for the Haines jump relative to the initial displacement time is almost insignificant. Further, Fig. 13 indicates that D increases with λ_c.

Snap-Off Rate in Porous Media

Equations (17) and (18) provide a basis for inferring the rate of snap-off in porous media and the effect of porous medium properties, such as permeability and capillary pressure. To scale pore-level phenomena so that macroscopic rates of foam generation by snap-off can be written, we invoke a statistical network description of porous media [39-41].

Minimal elements of a statistical description of porous-medium physics include size distribution functions for pore bodies and pore throats [40, 41]. Also, throat and body size correlations are typically constrained to insure that pore bodies with dimensions smaller than pore throats are not selected [41]. Foam generation and foam displacement of pore fluids is a drainage process, as demonstrated by Fig. 1. Thus, the pores that gas may enter at a given capillary pressure, P_c, are those having a throat radius greater than the drainage radius R_d. According to Eq. (1), R_d equals $2\sigma/P_c$ if the gas/liquid interface is hemispherical. In the simple models discussed below, we assume that all pores with a throat radius of R_d or greater are available to gas. More complicated analyses differentiate between pores where gas is allowed and where gas actually occupies the pore [40]. Neglecting occupancy statistics may overstate the probability of displacement somewhat, but at high P_c typical of strong foams at steady state we expect the allowed and occupied fractions to be nearly the same. Finally, we assume that the percolation threshold is exceeded so that multiphase flow is possible.

When this minimal description of a porous-medium network is combined with a pore-level description of foam physics, rate expressions for foam generation by snap-off may be developed. The regime of interest is that of strong foam flow where foams exhibit substantial pressure drops in the porous medium, ranging from 200 to 5000 kPa/m (O(10) to O(100) psi/ft). Within porous media, strong foams are characterized by a fairly dense pore-level spacing of lenses or lamellae, long-lived foam lamellae due to effective surfactant stabilization of the gas/liquid interface, *in-situ* regeneration of coalesced foam, intermittent mobilization of foam bubbles, and a high fraction of the gas-phase that is stationary, statistically, as trapped foam [20, 38, 42]. Flow is likely unsteady at the pore level because pore-level flow paths and pressure gradients for the gas and liquid phases fluctuate [39] and flow stream lines constantly evolve. Foam bubbles and lenses or lamellae only move, as described by Eq. (18), when the local pressure gradient is sufficient to keep them mobilized. Strong foam behavior translates to fluctuating, transient flow at the pore level, where pore-spanning lenses or lamellae alternate between periods of rest and motion.

For successful snap-off of a moving lens to occur within this backdrop of chaotic pore-level flow, a pore must exhibit a fairly small pore throat to body size ratio to ensure rapid

liquid accumulation, and posses sufficient liquid so that an unstable liquid collar may form near a pore throat. Yet the pore cannot be too highly constricted, so as to prevent lens mobilization. Liquid accumulation and mobilization do not necessarily occur simultaneously. A lens may generate but remain stationary for a period of time and then mobilize. Thus, we require pores with both a high, gas-phase pressure gradient and a lens forming geometry. We take the probability of a successful snap-off event as the product of the individual probabilities for liquid accumulation and lens mobilization:

$$\mathcal{P}_{so} = \mathcal{P}_a \mathcal{P}_d \tag{19}$$

where the probabilities, $\mathcal{P}$, are averaged over a representative sample of pore space.

The probability of an individual pore-level liquid accumulation event, p_a, and snap-off to a lens is presumed proportional to the frequency of liquid accumulation. To obtain the probability of accumulation, the pore-level probability is integrated over the fraction of pores that gas occupies and that also have sufficient pore throat to body size ratios and liquid saturation. Hence, the probability of accumulation within a network of pores is written:

$$\mathcal{P}_a = \int_{\lambda_d}^{\infty} \Gamma_c \left[\int_{\lambda_c/\lambda^*}^{\infty} \Gamma_b p_a \, d\lambda_b \right] d\lambda_c \tag{20}$$

where Γ_c is the distribution function describing the number fraction of pores with a given λ_c, Γ_b is the dimensionless, constrained, number fraction pore-body size distribution, and λ^* is the upper bound for the static criterion given in Eq. (7). Typically, pore throat and body sizes are made dimensionless by a single, characteristic pore dimension R_m. Since λ_d is inversely proportional to P_c according to Eq. (1), Eq. (20) explicitly reflects the capillary pressure or, equivalently, the liquid saturation dependence of snap-off via the Leverett J-function [43]. Moreover, Eq. (1) also identifies how the critical throat to body constriction ratio for each pore size varies with medium capillary pressure. As a porous medium becomes progressively drier, the capillary pressure rises; λ^* shrinks (*c.f.*, Table 1) and approaches zero. Thus, the lower integrand of the inner integral in Eq. (20) grows, the range of integration shrinks to

zero, and foam generation by snap-off ceases. Equation (17) also predicts that p_a decreases as the porous medium capillary pressure increases.

Additionally, the probability of an individual lens displacement event, p_d, is proportional to the frequency of lens displacement. The porous-medium averaged probability of lens displacement, $\mathcal{P}_d$, is found by integrating p_d over the fraction of gas-entered pores that are not too constricted for displacement events at a given gas-phase pressure drop:

$$\mathcal{P}_d = \int_{\lambda_d}^{\infty} \Gamma_c \left[\int_{\lambda_c}^{\lambda_c/g^*} \Gamma_b p_d \, d\lambda_b \right] d\lambda_c \tag{21}$$

where $g^*(\Delta\tilde{p})$ is the minimum pore throat to body ratio for lens mobilization at a given pressure gradient. As the pressure gradient increases, lens mobilization is possible over a wider range of pore sizes which is reflected in a reduced $g^*(\Delta\tilde{p})$; thus, a wider range of integration in Eq. (21). The inner integral in Eq. (21) correctly predicts that a lens in a wetting, unconstricted tube always flows given a nonzero gas-phase pressure drop.

To construct a porous-medium averaged rate expression for foam generation per unit volume of gas-occupied pore space, we substitute f_a and f_d given in Eqs. (17) and (18) for p_a and p_d in Eqs. (20) and (21), respectively. Second, the liquid pressure gradient is extracted from Ca_m, the gas pressure drops are converted to pressure gradients by division by L, and the result is dimensionalized by dividing both sides of the equation by the time scale $\mu R_m/\sigma$. Third, the result is divided by the mean gas volume per pore averaged over all pores, $\mathcal{V}_g$, to obtain the rate per unit volume of gas-occupied pore space (*c.f.*, [40, 41]). Lastly, since both the gas and liquid pressure gradients are independent of pore geometry and since the power-law exponent, η, is only a weak function of pore geometry according to Fig. 13, pressure gradient terms are moved outside the integral. That is,

$$r_g = k_1 |\nabla p_w| \left(|\nabla p_g| - |\nabla p_{g,T}| \right)^{\eta} + k_2 \left(|\nabla p_g| - |\nabla p_{g,T}| \right)^{\eta} \tag{22a}$$

where

$$k_1 = \frac{4L^{1+\eta}}{\mu \mathcal{V}_g}\left(\frac{R_m}{\sigma}\right)^{\eta}\left\{\int_{\lambda_d}^{\infty}\Gamma_c\left[\int_{\lambda_c/\lambda^*}^{\infty}\Gamma_b\, B\lambda_b\, d\lambda_b\right]d\lambda_c\right\}\left\{\int_{\lambda_d}^{\infty}\Gamma_c\left[\int_{\lambda_c}^{\lambda_c/g^*}\Gamma_b D\,\lambda_b{}^{\eta}\, d\lambda_b\right]d\lambda_c\right\} \quad (22b)$$

and

$$k_2 = \frac{L^{\eta}}{\mu \mathcal{V}_g}\left(\frac{R_m}{\sigma}\right)^{\eta-1}\left\{\int_{\lambda_d}^{\infty}\Gamma_c\left[\int_{\lambda_c/\lambda^*}^{\infty}\Gamma_b\, f_{a,o}\, d\lambda_b\right]d\lambda_c\right\}\left\{\int_{\lambda_d}^{\infty}\Gamma_c\left[\int_{\lambda_c}^{\lambda_c/g^*}\Gamma_b D\,\lambda_b{}^{\eta}\, d\lambda_b\right]d\lambda_c\right\} \quad (22c)$$

The proportionality constants, k_1 and k_2 reflect the number of foam germination sites as a function of pore size and geometry, the porous medium capillary pressure, and the gas-phase pressure gradient. For high water saturations, Eqs. (22) predict a large generation rate by snap-off. Figure 13 indicates that the power-law exponent, η, is roughly 2/3 for the pore throat to body aspect ratios typical of sandstones [44]. An example calculation of k_1 is given in the Appendix.

The mobilization pressure for lenses or foam lamellae within a network of pores is central to the frequency of displacement. Since the gas phase is dispersed as foam bubbles that are separated mainly by lamellae, it is not clear how to predict the threshold pressure gradient or the variation in g^* with pressure gradient and foam texture. A separate theory for lens or lamellae mobilization is needed that depends upon the permeability of the porous medium and the number density or texture of foam (*c.f.*, [45-51]). We leave the portion of the rate expression arising from lens displacement in its general power-law form. From the above theories for foam mobilization pressure gradients [45-51], we do expect, however, that the mobilization pressure gradient decreases inversely with R_c or the square root of permeability.

At the high pressure gradients characteristic of the steady flow of strong foam, the first term in Eq. (22a) dominates over the second, because large liquid-phase pressure gradients induce rapid snap-off as compared to static purely curvature driven accumulation of liquid according to Figs. 4, 5, 7, 11, and 12. In this case, r_g reduces to the form

$$r_g \approx k_1 |\nabla p_w| \left[|\nabla p_g| - |\nabla p_{g,T}|\right]^{\eta} \quad (23).$$

A variant of Eq (23) has been used elsewhere to successfully describe the experimentally observed gas and liquid velocity dependence of foam texture in consolidated sandstones [20, 21] with the constant k_1 fixed by history matching rather than evaluating Eq. (22b) directly.

DISCUSSION

Equations (22) and (23) do not account for existing lenses or lamellae that convect into a snap-off site where liquid is accumulating. If the rate of lens or lamella convection is too large, liquid accumulation at pore throats is prevented because the translating lenses or lamellae sweep the accumulating liquid out of the pore throat preventing the formation of lenses. However, in many foam displacements of interest [5, 18, 20, 52], strong foam coalescence forces apparently come into play before lamellae become so closely spaced that liquid accumulation is affected. Otherwise, the snap-off rate developed above must be compared to the lamellae convection rate to determine whether sufficient time exists for a lens to form before the accumulating liquid is swept out of the pore throat [17].

One of the major assumptions used in the proposed model of snap-off is that the rate of aqueous lens displacement out of a pore throat is greater than the rate of liquid accumulation. Thus, the two processes were decoupled and pore spanning lenses maintained constant volume. Figures 11 and 13 reveal that this is indeed a valid assumption. The frequencies of displacement and accumulation are on a common scaling and the frequency of lens displacement is roughly an order of magnitude greater than the frequency of accumulation.

Only snap-off in pores of square cross-section was presented quantitatively. Predicted flow-rate trends, though, apply equally to other cornered, cross-sectional pore shapes. First, different corner geometries shift t_a, but the trend of a linear increase in the frequency of liquid accumulation with the imposed liquid velocity through pore corners is maintained. For an equilateral triangle, t_a at a given Ca_m is slightly less than that for the square cross-section pore. More liquid is held in the corners of a triangular pore as compared to a square pore at the equilibrium entry curvature [16]. Therefore, in triangular geometries, liquid rearranges more quickly into a pore-spanning lens. Second, the drag-velocity scaling for the lens displacement portion of snap-off is independent of capillary geometry [28]. Geometry changes the proportionality constant; hence, it alters the actual time for displacement, but

not the velocity scaling found for t_d. Generally, the proportionality constant increases with the number of sides of a polygonally shaped pore. A circular pore represents the case of maximum drag. Since a pore of circular cross-section was employed for the displacement calculations, the actual lens displacement time for cornered pores is overestimated.

Finally, our analysis provides some insight into foam generation where gas and liquid-phase pressure gradients are very low. Figures 6 and 7 teach that accumulation of liquid and rearrangement into a pore-spanning lens occurs, provided that pores are strongly constricted, even in porous media where there is no liquid-phase pressure gradient and the average capillary pressure is quite high. Typical throat-to-body ratios range from 0.10 to 0.20 [44] in porous sandstones meeting our geometric criteria for highly constricted. Thus, even though pressure gradients are not sufficient to mobilize lenses, a portion of pore throats within a porous medium may be filled with lenses that snapped-off and now block gas flow. If surfactant is present at the interfaces of these lenses, they evolve into stationary foam lamellae if drained of wetting liquid. When such lamellae rupture, the porous medium has the opportunity to reform them provided sufficient liquid is present.

SUMMARY

A pore-level model for foam generation by snap-off of a gas thread in a constricted, cornered pore is presented. The important time scales analyzed are the time to accumulate liquid and form an aqueous lens, and subsequently the time to displace that lens so that snap-off can repeat.

A corner-flow hydrodynamic analysis of the formation of a wetting liquid collar reveals that under moderate imposed pressure gradients in the bulk wetting corner liquid, the time to accumulate sufficient liquid for snap-off decreases inversely with the wetting liquid velocity streaming through the pore corners. The time to accumulate liquid at a pore throat decreases rapidly with increased wetting liquid flow along pore corners. Symmetry boundary conditions applied in the pore bodies adjacent to a pore throat show that even though a pore may possess the critical pore throat to body ratio necessary for snap-off, sufficient liquid is not present to cause snap-off for pores with large pore constriction to body ratios. Snap-off proceeds all the way up to the static Roof snap-off criterion, when a pore is connected to an unimpeded source of wetting liquid.

A parameter central to the hydrodynamic analysis is the interfacial curvature at the pore boundary, or equivalently the porous-medium capillary pressure. We find that liquid accumulation continues even though pores are subject to strong capillary drainage forces.

Strongly constricted pores present a pore topology that drives liquid accumulation even when the porous-medium capillary pressure is high. Analogous to the Roof criterion, a static criterion determined by interfacial curvature at pore boundaries exists whereby the pore-throat to pore-body ratio must be sufficiently small for snap-off to occur.

A macroscopic momentum balance on the aqueous lens formed by collar rearrangement to a pore spanning lens shows that the frequency of lens displacement is not linear with the imposed pressure drop across a lens. The frequency of lens displacement scales with a power between 0.5 and 0.6 for pores with constriction radii between 0.15 and 0.4 when plotted versus the reduced pressure drop. The reduced pressure drop is the pressure drop across a lens minus the threshold pressure drop required to drive a lens through a pore constriction of a given geometry.

Simple network statistical arguments are used to scale the pore-level rates of liquid accumulation and lens displacement. Overall, the frequency or rate of foam generation by capillary snap-off increases linearly with the liquid-phase pressure gradient, while the rate of generation increases according to a power-law relationship with imposed gas-phase pressure gradient.

ACKNOWLEDGMENT

This work was supported by the Assistant Secretary for Fossil Energy, Office of Oil, Gas, and Shale Technologies of the U. S. Department of Energy, under contract No. DE-AC03-76FS00098 to the Lawrence Berkeley National Laboratory of the University of California.

NOMENCLATURE

a	radius of interfacial curvature, m
A	cross-sectional area, m^2
B	proportionality constant in the expression for frequency of accumulation
Ca	capillary number
Ca_m	modified capillary number
C_m	mean interfacial curvature, m^{-1}
D	proportionality constant in the expression for lens displacement
D_f	three-phase contact-line drag force, N
f	frequency, s^{-1}
F_D	viscous drag force, N

F_p pressure force exerted by pore wall, N

g aspect ratio for lens mobilization

G gamma function

h dimensionless axial position for lens displacement calculations

$k_{1,2}$ constants in rate expression for foam generation by capillary snap-off, $s^{-1}\ m^{\eta-2}\ Pa^{-(1+\eta)}$ and $s^{-1}\ m^{\eta-3}\ Pa^{-\eta}$, respectively

L constriction wavelength, m

Oh Ohnesorge number

p phase pressure, Pa

P_c capillary pressure, Pa

p probablility of a successful, pore-level accumulation or displacement event

$\mathcal{P}$ probability averaged over a representative volume of porous media

q_w volumetric wetting liquid flow rate, m^3/s

r radial coordinate, m

r_g rate of foam generation by snap-off, $m^{-3}s^{-1}$

R radius of largest inscribed circle in a pore cross section, m

$S_{1,2}$ dimensionless pore shape integrals

t time, s

t_a dimensionless liquid accumulation time

t_c characteristic time for liquid accumulation, s

t_d dimensionless lens displacement time

U average axial lens velocity, m/s

v_z axial velocity profile, m/s

V lens volume, m^3

$\mathcal{V}_g$ volume of gas-occupied pore space in network model, m^3

z axial distance along a constricted pore, m

Greek Letters

α proportionality constant for contact-line drag

β dimensionless flow resistance along a corner

η power-law exponent describing f_d

Γ dimensionless pore-size distribution function

κ dimensionless interfacial radius of curvature

λ dimensionless pore radius

μ wetting liquid viscosity, Pa-s

ρ wetting liquid density, kg/m^3

σ surface tension, N/m

τ dimensionless time

ω angle between r and a in a constricted tube

ξ dummy variable of integration

ζ dimensionless axial distance

Superscripts

~ dimensionless quantity

* critical pore throat to body aspect ratio

Subscripts

1,2 denote orthogonal radii of curvature

1,2 denote location of surfaces for momentum balance

a liquid accumulation

b body, boundary

c constriction

d lens displacement, drainage

e equilibrium

g gas phase

λ transverse radius of curvature

m characteristic dimension

o no pressure gradient is imposed

so snap-off

T threshold pressure drop

w wetting phase

APPENDIX

A sample evaluation of Equation (22b) as a function of λ_d is provided here. Integration is performed with the trapezoidal rule. The necessary size distribution functions, functional forms for B and D, and values of the parameters g*, η, and $\widetilde{C}_{m,e}$, are given in Table A1.

The pore-throat size distribution is represented by a two parameter gamma distribution, Eq. (A1), and the body size is described by a constrained gamma distribution. Equation (A2) ensures that each pore has a body size that equals or exceeds the corresponding throat size. In both Eqs. (A1) and (A2), G is the gamma function. Pore dimensions λ_c and λ_b are made dimensionless by the common characteristic dimension R_m. Hence, if we need the ratio of R_c upon R_b for a given pore, we substitute λ_c/λ_b.

The parameter B, which describes the increase in the frequency of liquid accumulation with increasing liquid phase pressure gradient, is represented by the simple relation in Eq. (A3) where B is a nonzero constant if λ_c/λ_b is less than λ^* as given by Eq. (7) and is zero otherwise. The value of B in Table A1 is the average value of the slopes found on Fig. 11. Next, an analysis of D for the constriction sizes portrayed in Fig. 13 reveals that D decreases linearly with λ_c/λ_b. Equation (A4) gives the exact expression for this line.

The minimum pore throat to body ratio for lens mobilization , g*, is set to consecutive values of 0.15, 0.20, 0.25, and 0.30 to simulate a decreasing gas-phase pressure gradient, while the power-law exponent, η is set to 2/3. Finally, the dimensionless entry curvature for each pore, $\widetilde{C}_{m,e}$, is set to 1.89 to represent pores with a square cross section.

Figure A1 presents a dimensionless k_1 versus λ_d^{-1} for different values of g*. The inverse of the drainage radius is chosen because it is proportional to capillary pressure. For square pores undergoing liquid drainage, the capillary pressure equals $1.89\sigma/\lambda_d R_m$, and the x-axis of Fig. A1 spans from a P_c of zero to roughly 12 kPa for σ = 32mN/m and a characteristic pore diameter of 100 μm. As expected, the number of foam germination sites embodied by k_1 is quite small when the capillary pressure is close to zero, increases rapidly and peaks as the largest pores are desaturated, and then declines rather slowly as λ_d^{-1} increases further and pores become progressively drier. Further, as g* increases, the likelihood of lens mobilization decreases, and k_1 decreases.

REFERENCES

1. Moritas, G., "Enhanced Oil Recovery Report," *Oil and Gas Journal*, 88 (1990) 49-82.

2. Mohammadi, S.S., D.C. Van Slyke, and B.L. Ganong, "Steam-Foam Pilot Project in Dome-Tumbador, Midway-Sunset Field," *Soc. Pet. Eng. Res. Eng.*, 4 (1989) 7-16.

3. Patzek, T.W. and M.T. Koinis, "Kern River Steam-Foam Pilots," *J. Petr. Tech.*, 42 (1990) 496-503.

4. Friedmann, F., M.E. Smith, W.R. Guice, J.M. Gump, and D.G. Nelson, "Steam-Foam Mechanistic Field Trial in the Midway-Sunset Field," *Soc. Pet. Eng. Res. Eng*, 9 (1994) 297-304.

5. Ettinger, R.A. and C.J. Radke, "Influence of Foam Texture on Steady Foam Flow in Berea Sandstone," *Soc. Pet. Eng. Res.Eng.*, 7 (1992) 83-90.

6. Ettinger, R.A., *Foam Flow Resistance in Berea Sandstone,* M.S. Thesis, University of California, Berkeley, 1989.

7. Chambers, K.T. and C.J. Radke, "Capillary Phenomena in Foam Flow Through Porous Media," in *Interfacial Phenomena in Petroleum Recovery*, N.R. Morrow, (Ed.), Marcel Dekker Inc., New York, 1991, 191-255.

8. Mast, R.F., "*Microscopic Behavior of Foam in Porous Media,*" , SPE 3997, presented at the the 47th SPE Annual Meeting, San Antonio, TX, October, 1972.

9. Owete, O.S. and W.E. Brigham, "Flow Behavior of Foam: A Porous Micromodel Study," *Soc. Pet. Eng. Res. Eng.*, 2 (1987) 315-323.

10. Ransohoff, T.C. and C.J. Radke, "Mechanisms of Foam Generation in Glass-Bead Packs," *Soc. Pet. Eng. Res. Eng.*, 3 (1988) 573-585.

11. Goren, S.L., "The Instability of an Annular Thread of Fluid," *J. Fluid Mech.*, 12 (1962) 309-319.

12. Hammond, P.S., "Nonlinear Adjustment of a Thin Annular Film of Viscous Fluid Surrounding a Thread of Another Within a Circular Cylindrical Pipe," *J Fluid Mech.*, 137 (1983) 363-384.

13. Gauglitz, P.A. and C.J. Radke, "An Extended Evolution Equation for Liquid Breakup in Cylindrical Capillaries," *Chem. Eng. Sci.*, 43 (1988) 1457-1465.

14. Aul, R.W. and W.L. Olbricht, "Stability of a thin annular film in pressure-driven low-Reynolds-number flow through a capillary," *J. Fluid Mech,*, 215 (1990) 585-595.

15. Roof, J.G., "Snap-Off of Oil Droplets in Water-Wet Pores," *Soc. Petr. Eng. J.*, 10 (1970) 85-90.

16. Ransohoff, T.C., P.A. Gauglitz, and C.J. Radke, "Snap-Off of Gas Bubbles in Smoothly Constricted Noncircular Capillaries," *Am. Inst. Chem. Eng. J*, 33 (1987) 753-765.

17. Falls, A.H., G.J. Hirasaki, T.W. Patzek, P.A. Gauglitz, D.D. Miller, and T. Ratulowski, "Development of A Mechanistic Foam Simulator: The Population Balance and Generation By Snap-Off," *Soc. Pet. Eng. Res. Eng.*, 3 (1988) 884-892.

18. Persoff, P., C.J. Radke, K. Pruess, S.M. Benson, and P.A. Witherspoon, "A Laboratory Investigation of Foam Flow in Porous Media at Elevated Pressure," *Soc. Pet. Eng. Res. Eng.*, 6 (1991) 365-371.

19. Hirasaki, G.J. and J.B. Lawson, "Mechanisms of Foam Flow in Porous Media: Apparent Viscosity in Smooth Capillaries," *Soc. Pet. Eng. J.*, 25 (1985) 176-190.

20. Kovscek, A.R. and C.J. Radke, "Fundamentals of Foam Transport in Porous Media," in *Foams in the Petroleum Industry*, L.L. Schramm, (Ed.), American Chemical Society, Washington, D.C., 1994, 115-163.

21. Kovscek, A.R., T. W. Patzek, and C.J. Radke, "A Mechanistic Population Balance Model For Transient and Steady-State Foam Flow in Boise Sandstone," *Chem. Eng. Science*, 50 (1995) to appear.

22. Mayer, R.P. and R.A. Stowe, "Mercury Porosimetry--Breakthrough Pressure for Penetration Between Packed Spheres," *J. Coll. Interface. Sci*, 20 (1965) 893-911.

23. Wong, H., S. Morris, and C.J. Radke, "Three-Dimensional Menisci in Polygonal Capillaries," *J Coll. and Interface. Sci*, 148 (1992) 317-336.

24. Wong, H., S. Morris, and C.J. Radke, "Two-Dimensional Menisci in Non-Axisymmetric Capillaries," *J. Coll. Interface Sci*, 148 (1992) 284-287.

25. Legait, B., "Laminar Flow of Two Phases through a Capillary Tube with Variable Square Cross Section," *J Coll. Interface. Sci.*, 96 (1983) 28-38.

26. Dullien, F.A.L., *Porous Media: Fluid Transport and Pore Structure*, Academic Press, New York, 1979.

27. Gauglitz, P.A. and C.J. Radke, "The Dynamics of Liquid Film Breakup in Constricted Cylindrical Capillaries," *J. Coll. Interface. Sci*, 134 (1990) 14-40.

28. Wong, H., C.J. Radke, and S. Morris, "The Motion of Long Bubbles in Polygonal Capillaries: II. Drag, Fluid Pressure, and Fluid Flow," *J. Fluid Mech.*, 292 (1995) 95-110.

29. Wong, H., C.J. Radke, and S. Morris, "The Motion of Long Bubbles in Polygonal Capillaries: I. Thin Films," *J. Fluid Mech.*, 292 (1995) 71-95.

30. Ransohoff, T.C. and C.J. Radke, "Laminar Flow of a Wetting Liquid along the Corners of a Predominantly Gas-Occupied Noncircular Pore," *J. Coll. Interface. Sci*, 121 (1988) 392-499.

31. Kovscek, A.R., *Foam Displacement in Porous Media: Experiment and Mechanistic Prediction by the Population Balance Method,* Ph.D Thesis, University of California, Berkeley, 1994.

32. Gauglitz, P.A. and C.J. Radke, "Dynamics of Haines Jumps for Compressible Bubbles in Constricted Capillaries," *Am. Inst. Chem. Eng. J*, 35 (1989) 230-240.

33. Denn, M.M., *Process Fluid Mechanics*, Ch. 5, Prentice-Hall Inc., Englewood Cliffs, N.J., 1980.

34. Wong, H., *The Motion of a Long Bubble in Polygonal Capillaries at Low Capillary Numbers,* University of California, Berkeley, 1992.

35. Bretherton, F.P., "The Motion of Long Bubbles in Tubes," *J. Fluid Mech.*, 10 (1961) 166-188.

36. Morrow, N.R., "Physics and Thermodynamics of Capillary Action in Porous Media," *Ind. Eng. Chem.*, 62 (1970) 32-56.

37. Hildebrand, F.B., *Introduction to Numerical Analysis 2nd Ed.*, Ch. 6, Mc Graw-Hill, New York, 1974.

38. Friedmann, F., W.H. Chen, and P.A. Gauglitz, "Experimental and Simulation Study of High-Temperature Foam Displacement in Porous Media," *Soc. Pet. Eng. Res. Eng.*, 6 (1991) 37-45.

39. Mohanty, K.K., H.T. Davis, and L.E. Sriven, "Physics of Oil Entrapment in Water-Wet Rock," *Soc. Pet. Eng. Res. Eng.*, 2 (1987) 113-128.

40. Heiba, A.A., S. Sahimi, L.E. Scriven, and H.T. Davis, "Percolation Theory of Two-Phase Relative Permeability," *Soc. Pet. Eng. Res. Eng.*, 7 (1992) 123-132.

41. Chou, S.I., "*Percolation Theory of Foam in Porous Media,*" , SPE/DOE 20239, presented at the 7th SPE/DOE Symposium on Enhanced Oil Recovery, Tulsa, OK, April, 1990.

42. Gillis, J.V. and C.J. Radke, "*A Dual-Gas Tracer Technique for Determining Trapped Gas Saturation During Steady Foam Flow in Porous Media,*" , SPE 20519, presented at the 65th SPE Annual Technical Conference, New Orleans, LA, September, 1990.

43. Leverett, M.C., "Capillary Behavior in Porous Solids," *Trans., AIME*, 142 (1941) 152-169.

44. Wardlaw, N.C., Y. Li, and D. Forbes, "Pore-Throat Size Correlation From Capillary Pressure Curves," *Transport in Porous Media*, 2 (1987) 597-614.

45. de Gennes, P.G., "Conjectures on Foam Mobilization," *Revue De L'Institut Francais Du Pe'trol*, 47 (1992) 249-254.

46. Hanssen, J.E., "Foam as a Gas-Blocking Agent in Petroleum Reservoirs. II: Mechanisms of Gas Blockage," *Journal of Petroleum Science & Engineering*, 10 (1993) 135-156.

47. Flumerfelt, R.W. and J. Prieditis, "Mobility of Foam in Porous Media," in *Surfactant Based Mobility Control: Progress in Miscible-Flood Enhanced Oil Recovery*, D.H. Smith, (Ed.), ACS Books, Washington, D.C., 1988, 295-325.

48. Rossen, W.R., "Theory of Mobilization Pressure Gradient of Flowing Foams in Porous Media: I. Incompressible Foam," *J. Coll. Interface. Sci.*, 136 (1990) 1-16.

49. Rossen, W.R., "Theory of Mobilization Pressure Gradient of Flowing Foams in Porous Media: II. Effect of Compressibility," *J. Coll. Interface. Sci*, 136 (1990) 17-37.

50. Rossen, W.R., "Theory of Mobilization Pressure Gradient of Flowing Foams in Porous Media: II. Asymmetric Lamella Shapes," *J. Coll. Interface. Sci.*, 136 (1990) 38-53.

51. Rossen, W.R. and P.A. Gauglitz, "Percolation Theory and Mobilization of Foams in Porous Media," *Am. Inst. Chem. Eng. J.*, 37 (1990) 1176-1188.

52. Khatib, Z.I., G.J. Hirasaki, and A.H. Falls, "Effects of Capillary Pressure on Coalescence and Phase Mobilities in Foams Flowing Through Porous Media," *Soc. Pet. Eng. Res. Eng.*, 3 (1988) 919-926.

Table 1: Critical aspect ratios for square tube calculations.

$P_{c,b}/P_{c,e}$	λ^*
1	0.53
1.1	0.48
1.2	0.44
1.4	0.38
1.8	0.29

Table A1: Equations and parameter values for sample calculation.

Quantity, Symbol		Equation
throat distribution function, Γ_c	$\Gamma_c = \frac{\lambda_c^{0.5} \exp(-\lambda_c)}{G(1.5)}$	A1
constrained body distribution function, Γ_b	$\Gamma_b = \begin{cases} 0, & \lambda_b < \lambda_c \\ \frac{\lambda_b^2 \exp(-\lambda_b)}{G(3)\int_{\lambda_c}^{\infty} \lambda_b^2 \exp(-\lambda_b)/G(3)\, d\lambda_b}, & \lambda_b \geq \lambda_c \end{cases}$	A2
proportionality constant for the frequency of accumulation, B	$B = \begin{cases} 1.4\,\text{E-6}, & \frac{\lambda_c}{\lambda_b} < \lambda^* \\ 0, & \frac{\lambda_c}{\lambda_b} \geq \lambda^* \end{cases}$	A3
proportionality constant for the frequency of lens displacement, D	$D = 0.0080937 - \frac{0.00096142}{\lambda_c/\lambda_b}$	A4
g^*	0.15, 0.20, 0.25, and 0.30	
η	0.66	
$\widetilde{C}_{m,e}$	1.89	

FIGURE CAPTIONS

Figure 1: Sequence of events leading to foam generation by snap-off (a) entry of unshaded gas into a liquid filled pore throat, (b) accumulation of aqueous liquid at the pore throat into a collar, (c) rearrangement of aqueous liquid to a pore-spanning lens, and (d) displacement of lens from pore throat.

Figure 2: Typical geometry of a capillary constriction.

Figure 3: Cross sections of (a) realistic pores in reservoir media, and (b) model square pores. Thin wetting films line pore walls.

Figure 4: Dimensionless time for liquid accumulation into a pore neck to cause snap-off for varying constriction ratios. The effect of imposed liquid-phase pressure gradient with constant curvature boundaries is illustrated.

Figure 5: Dimensionless time for liquid accumulation into a pore neck to cause snap-off for varying constriction ratios. The effect of imposed liquid-phase pressure gradient with no-flux boundaries is illustrated.

Figure 6: Dimensionless time for liquid accumulation into a pore neck to cause snap-for varying constriction ratios. The effect of interfacial curvature at the pore boundary is illustrated at $Ca_m = 0$.

Figure 7: Dimensionless time for liquid accumulation into a pore neck to cause snap-off for varying constriction ratios. The effect of liquid-phase pressure gradient is illustrated for $P_{c,b}/P_{c,e} = 1.4$.

Figure 8: An aqueous lens located within a periodically constricted tube.

Figure 9: Dimensionless lens displacement time versus distance at the rear meniscus wall contact in a periodically constricted cylindrical pore.

Figure 10: Dimensionless time to displace a lens for varying constriction ratios. The effect of increasing pressure drop across the lens is illustrated.

Figure 11: Dimensionless frequency of liquid accumulation into a pore constriction as a function of the modified capillary number over a range of constriction radii at $P_{c,b}/P_{c,e} = 1.0$.

Figure 12: Dimensionless frequency of liquid accumulation into a pore constriction as a function of the modified capillary number over a range of pore boundary curvatures.

Figure 13: Dimensionless frequency of lens displacement out of a pore constriction as a function of reduced pressure drop.

Figure A1: Dimensionless rate constant for capillary snap-off as a function of inverse drainage radius.

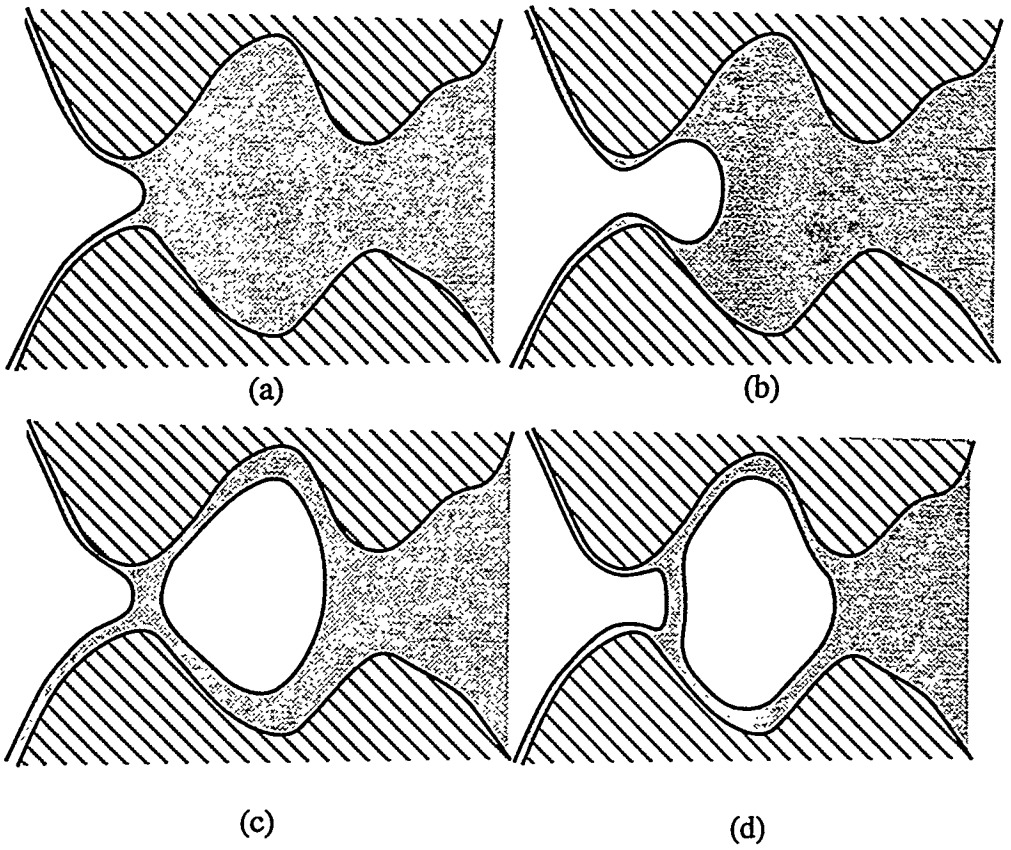

Fig. 1 Kovscek and Radke

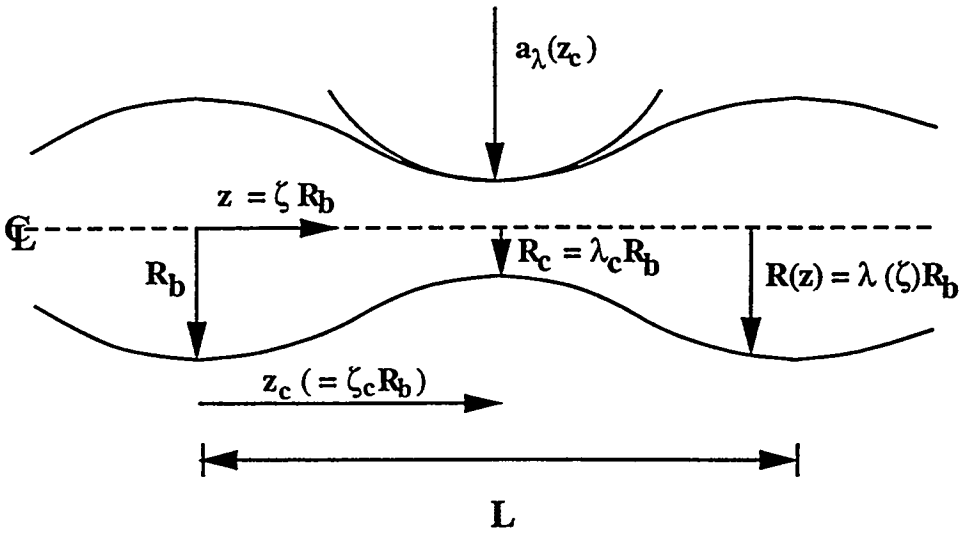

Fig. 2 Kovscek and Radke

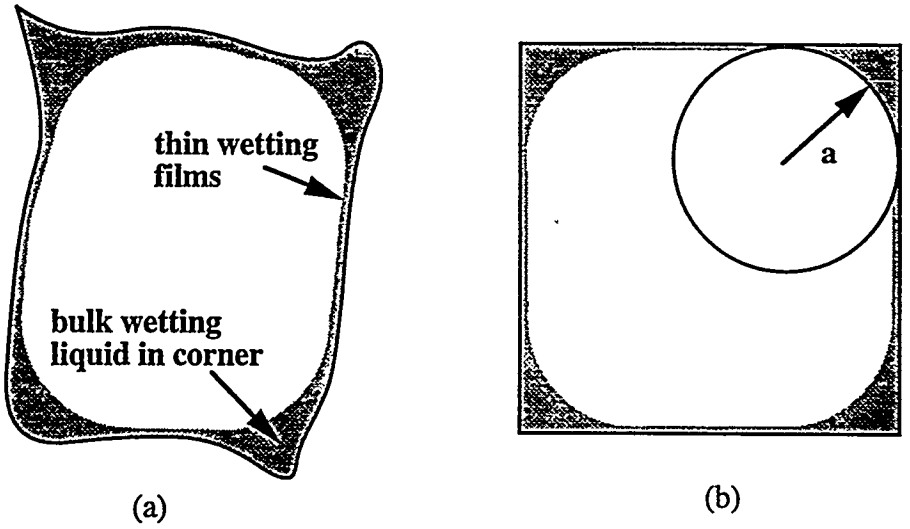

Fig. 3 Kovscek and Radke

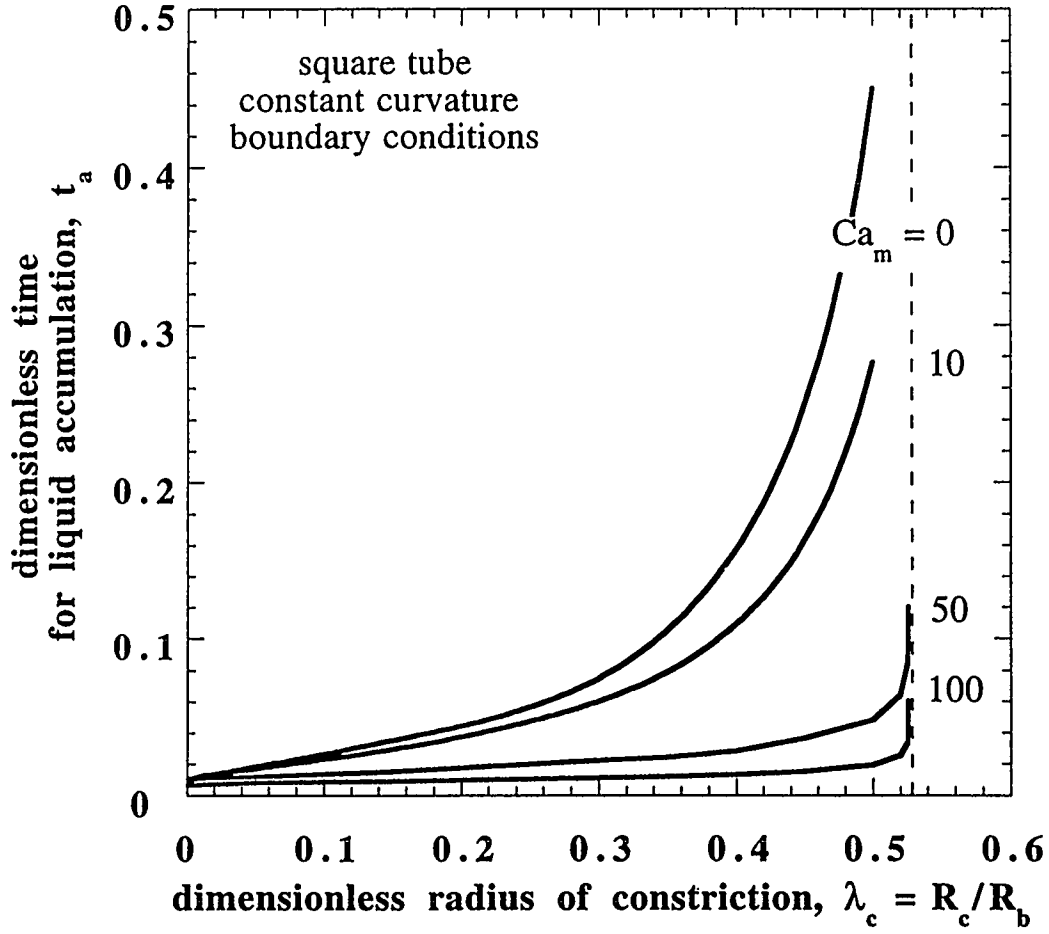

Fig. 4 Kovscek and Radke

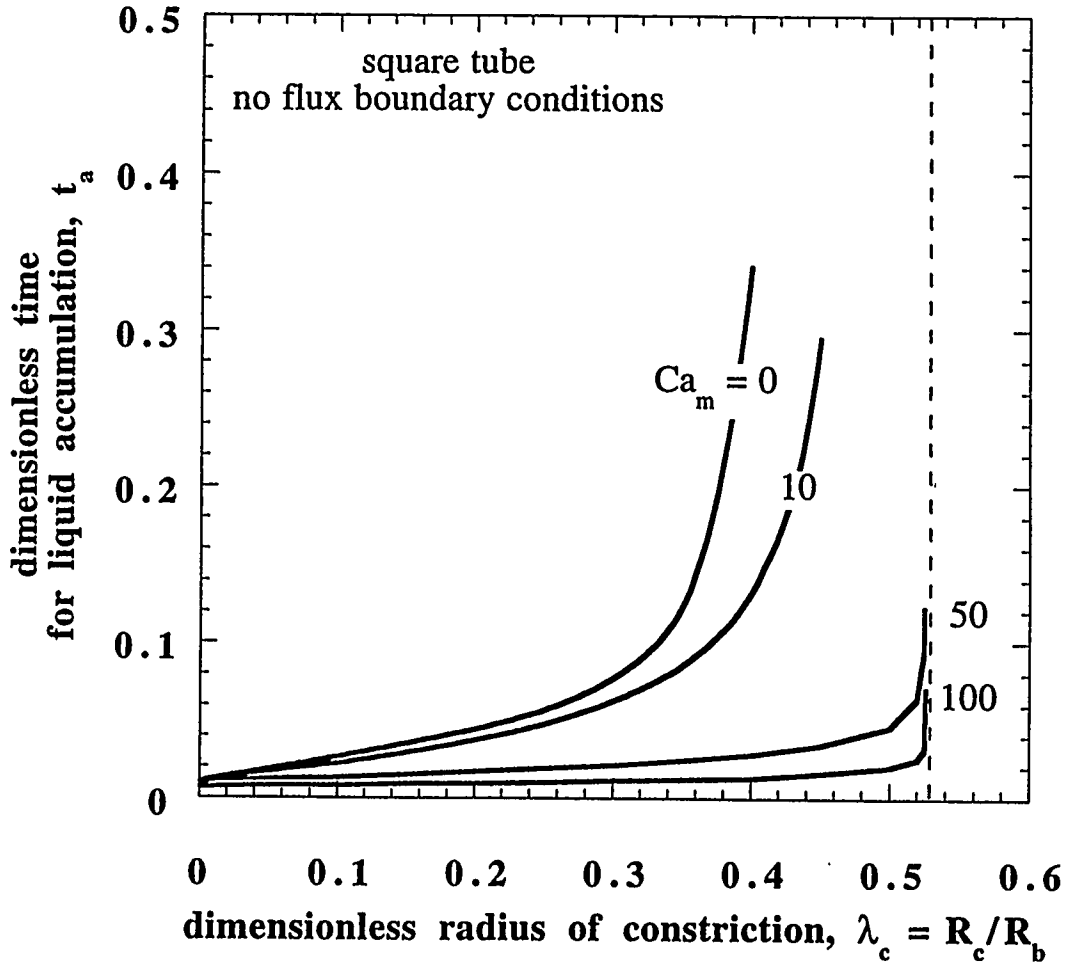

Fig. 5 Kovscek and Radke

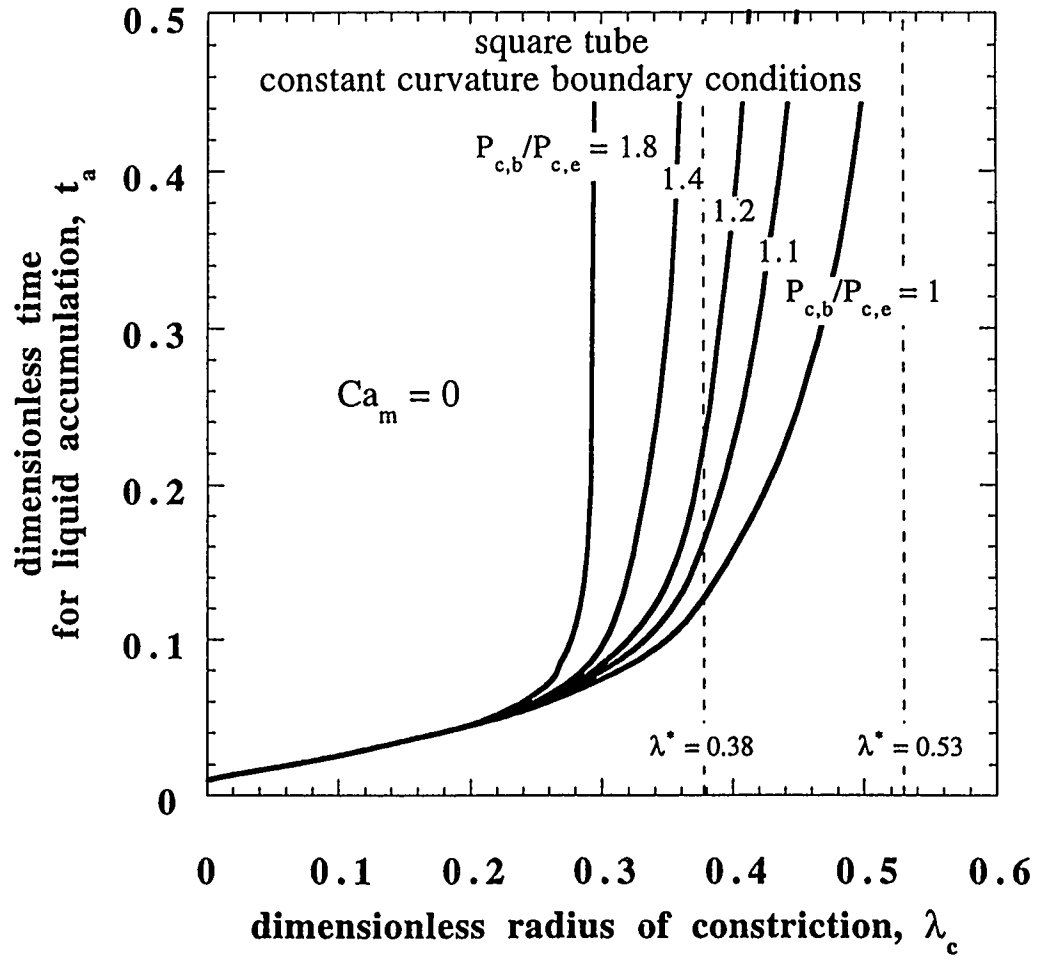

Fig. 6 Kovscek and Radke

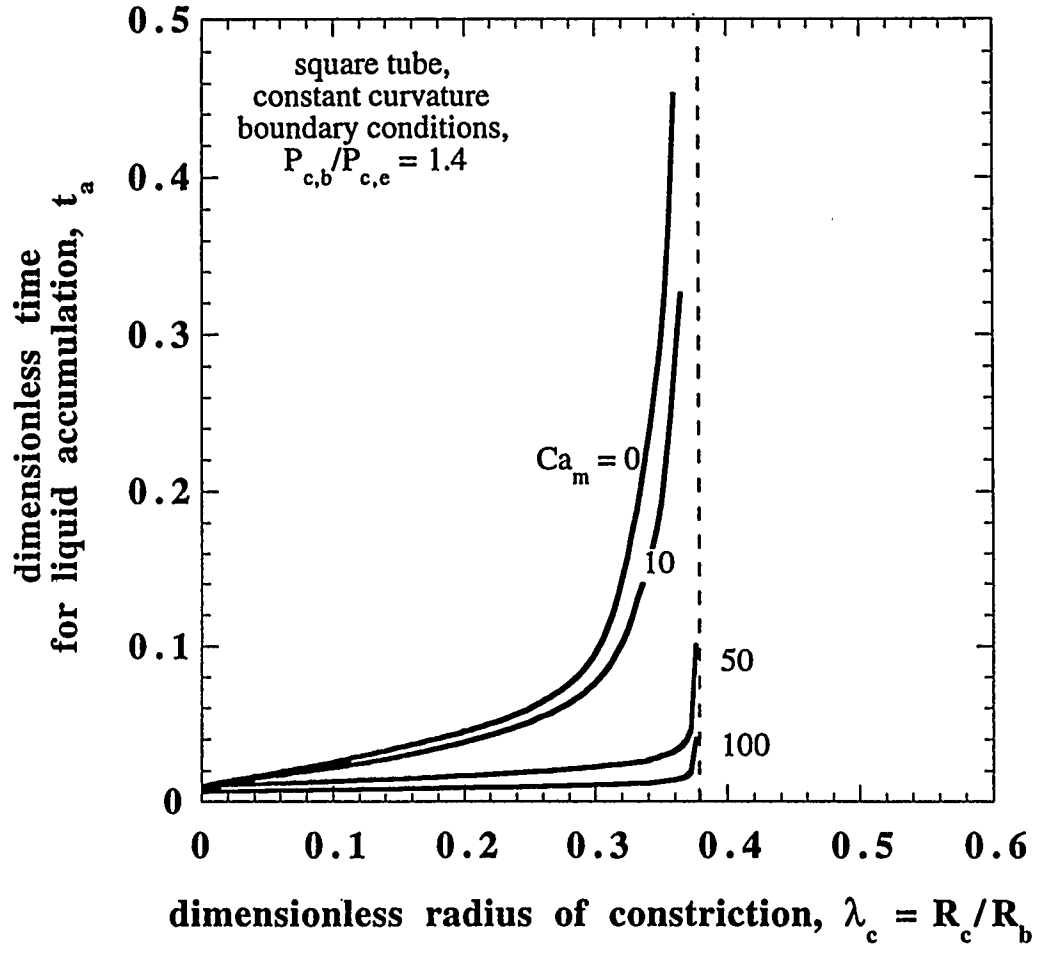

Fig. 7 Kovscek and Radke

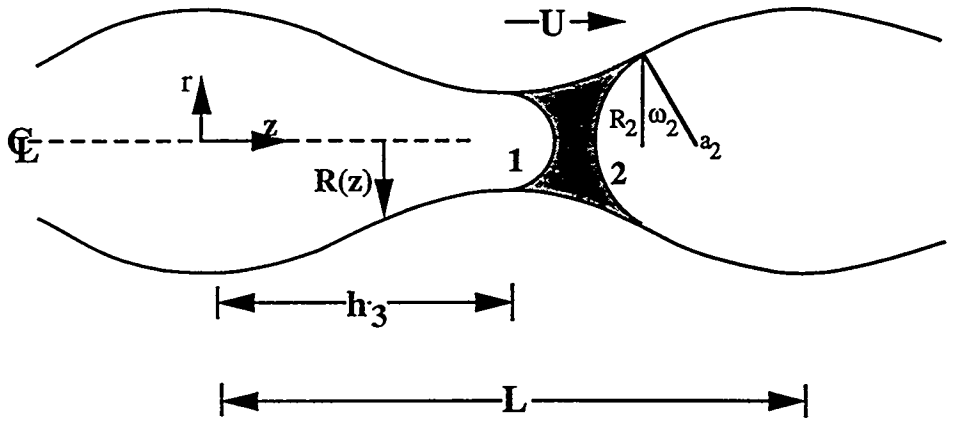

Fig. 8 Kovscek and Radke

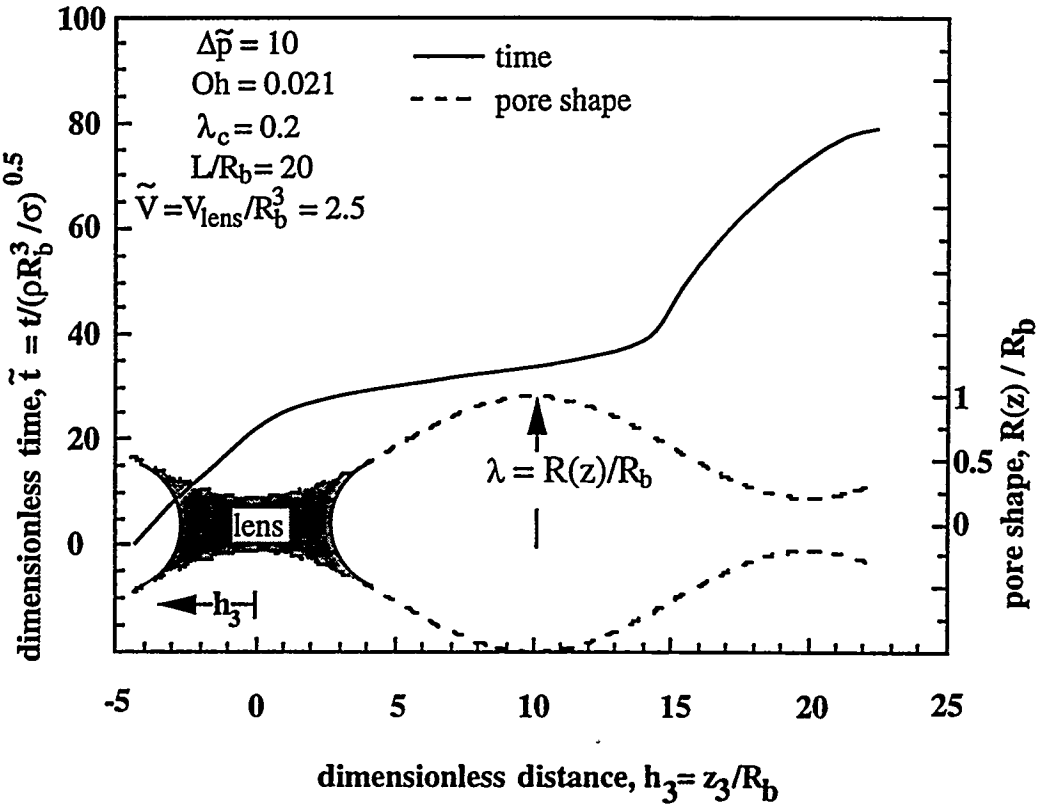

Fig. 9 Kovscek and Radke

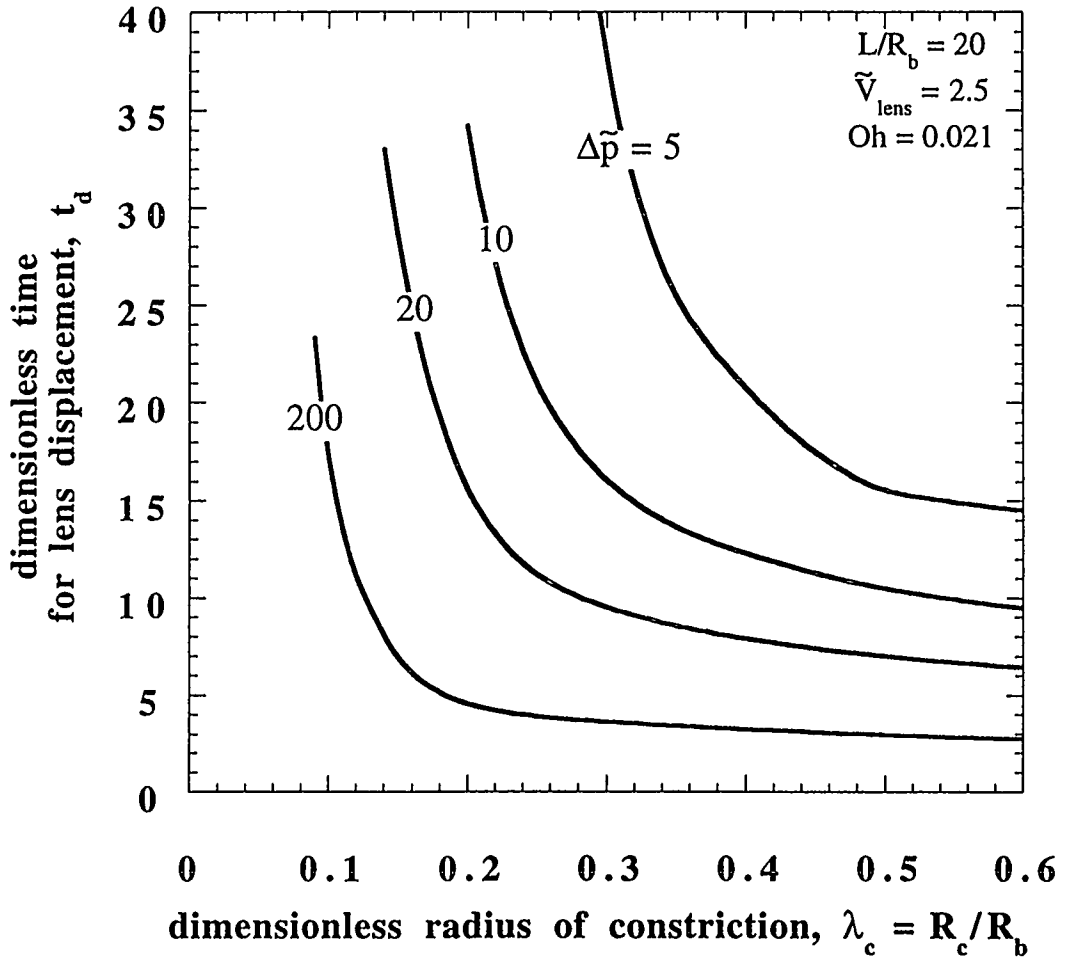

Fig. 10 Kovscek and Radke

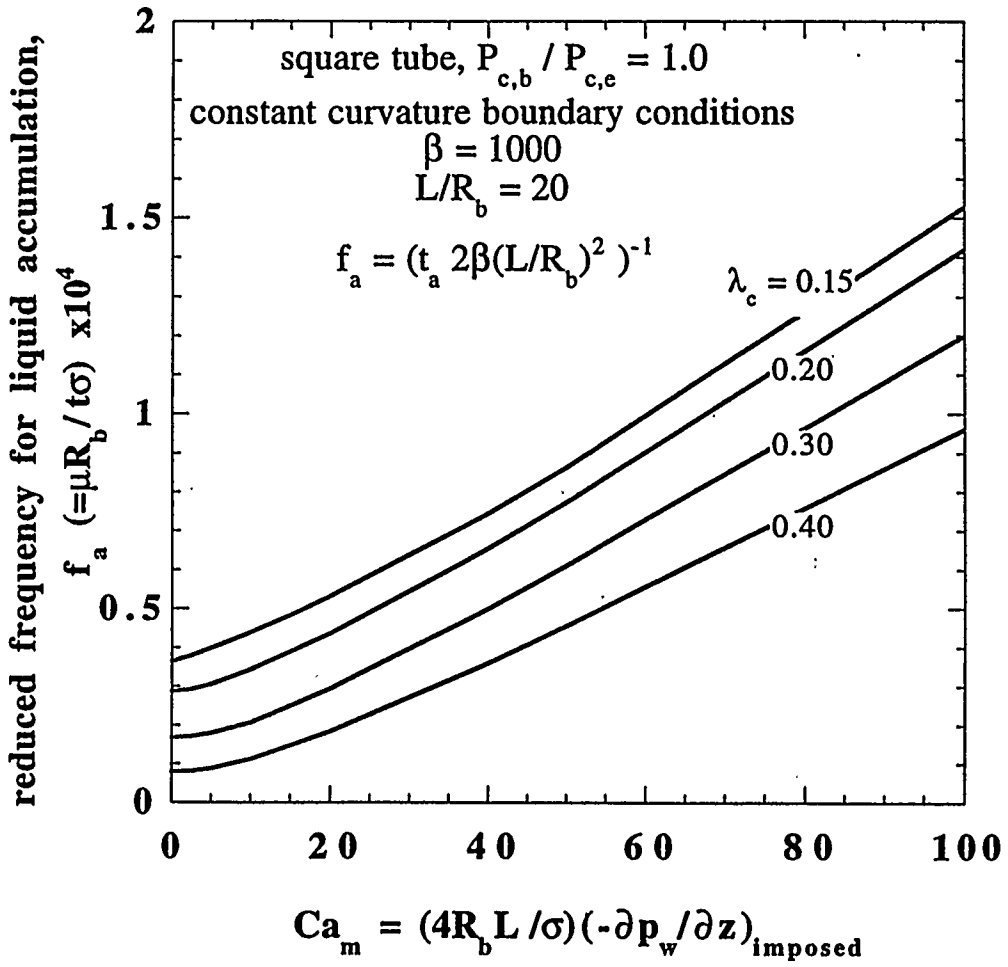

Fig. 11: Kovscek and Radke

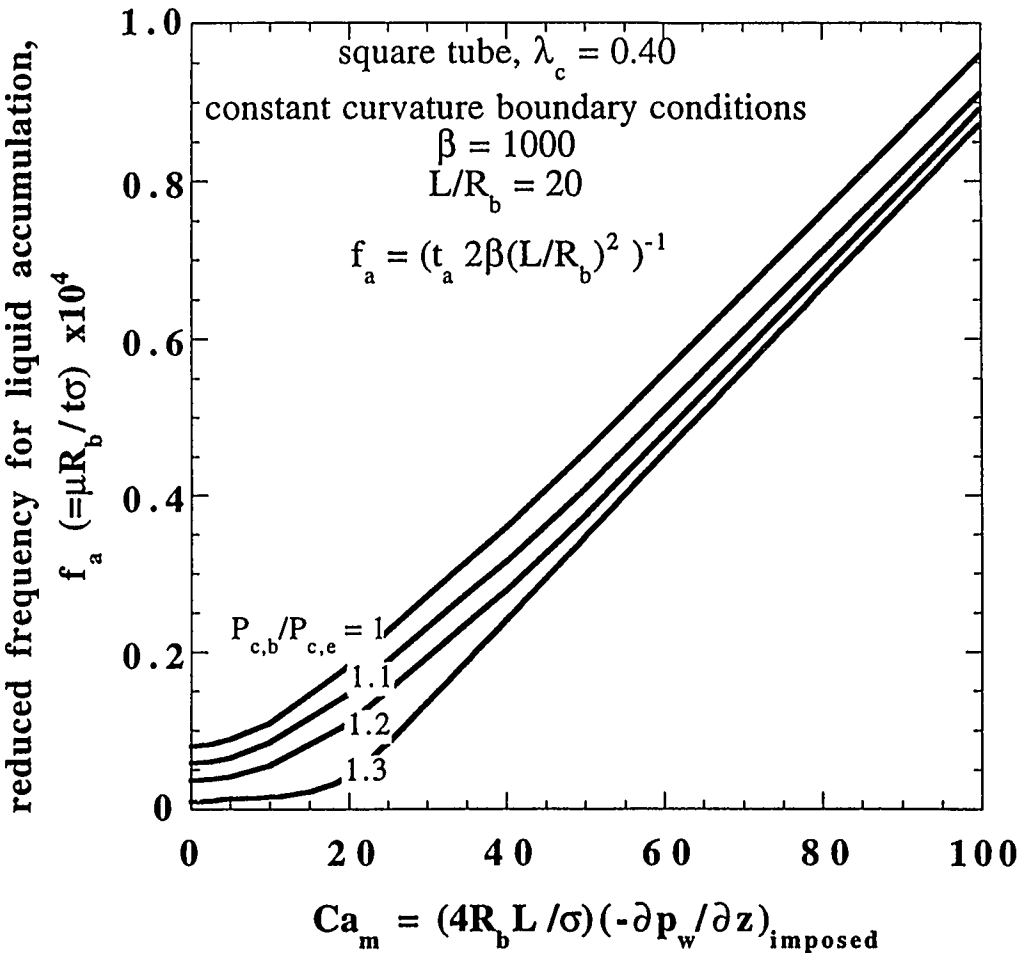

Figure 12: Kovscek and Radke

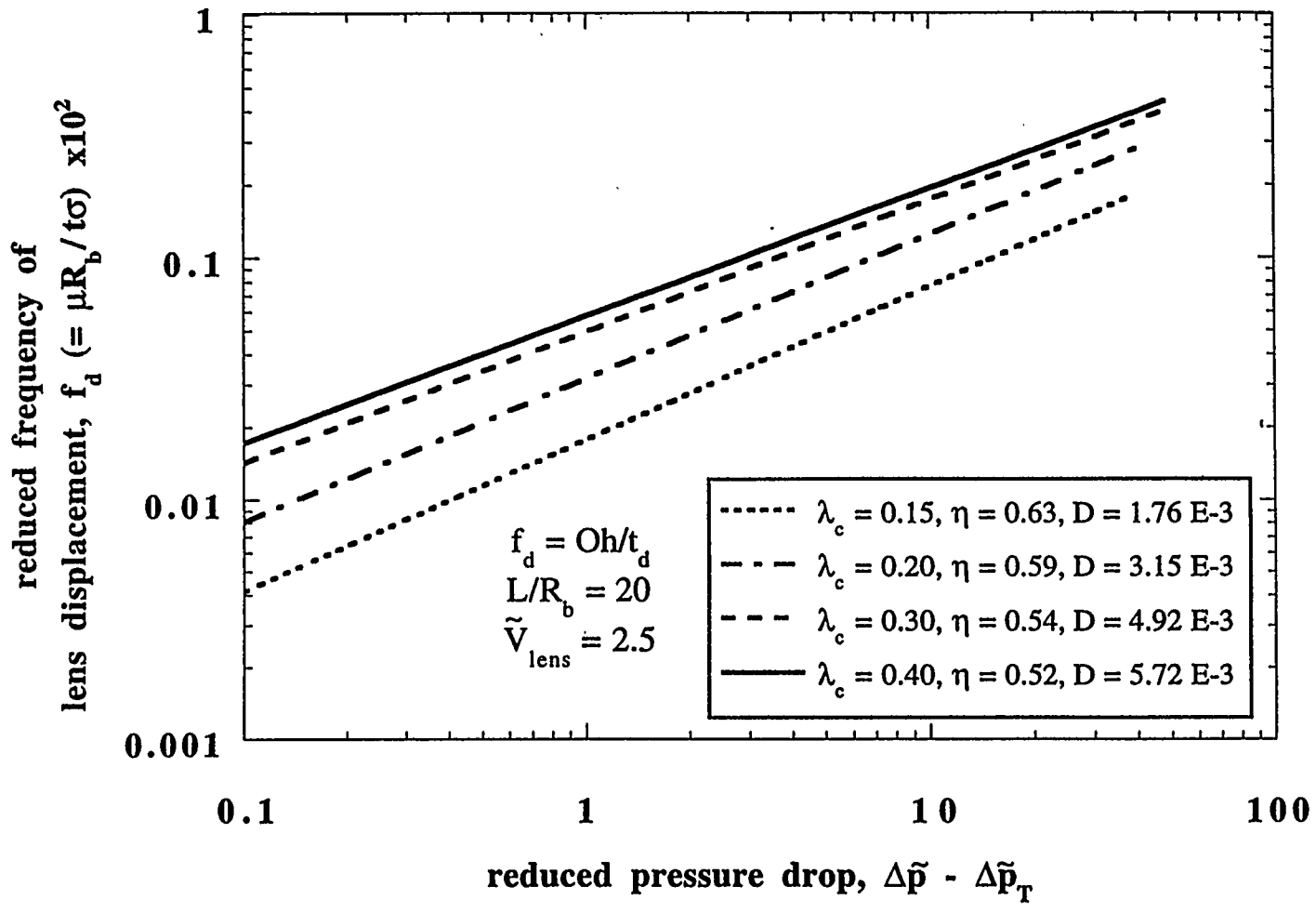

Fig. 13 Kovscek and Radke

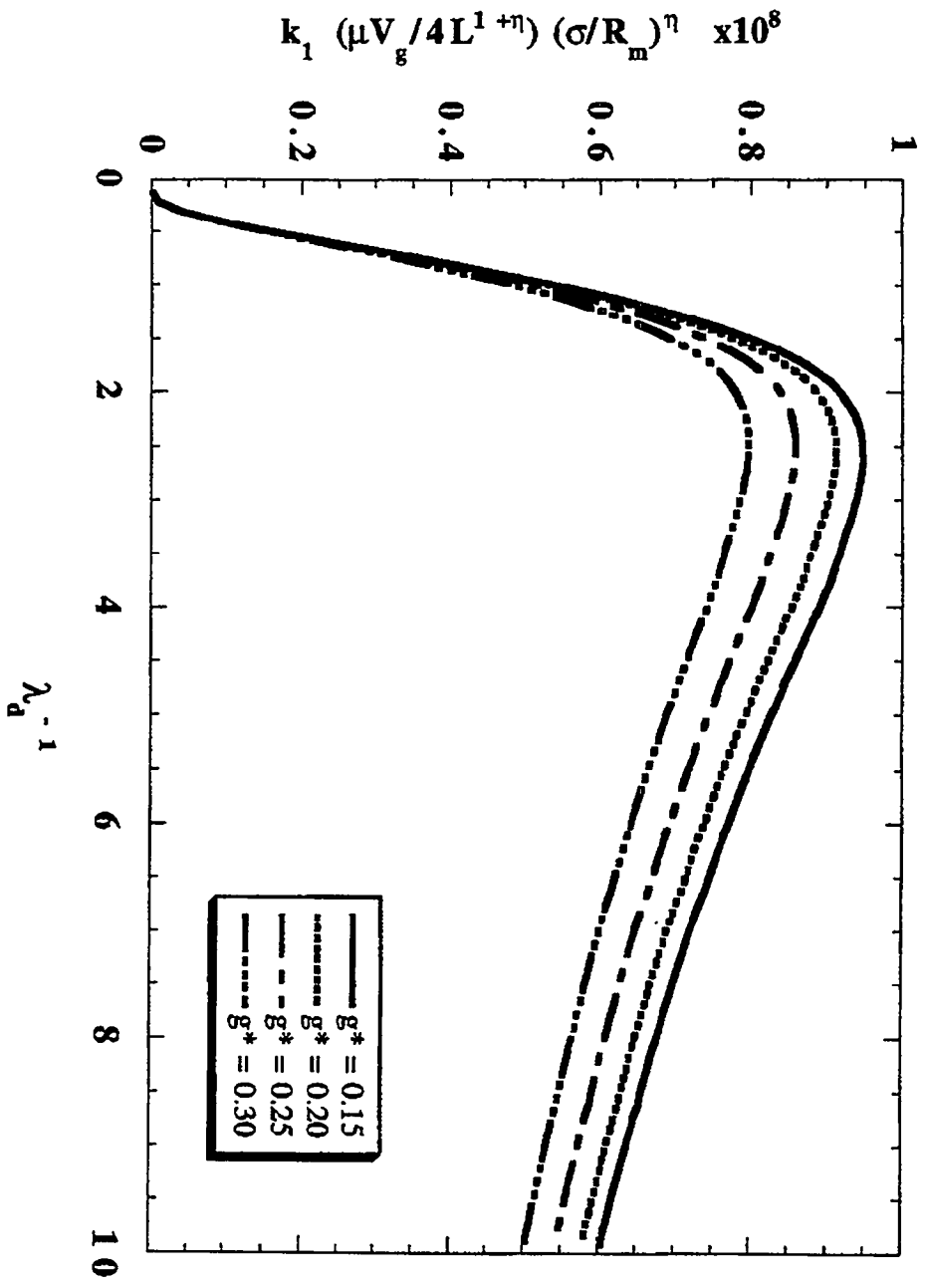

Fig. A1 Kovscek and Radke

☆U.S. GOVERNMENT PRINTING OFFICE: 1996 - 760-032/40007